Monthly Notices of the ROYAL ASTRONOMICAL SOCIETY

MNRAS **496,** 5482–5502 (2020) doi:10.1093/mnras/staa1858
Advance Access publication 2020 June 26

Non-linear dynamical tides in white dwarf binaries

Hang Yu [1,2]★ Nevin N. Weinberg [1] and Jim Fuller [2]

[1]*Department of Physics, and MIT Kavli Institute, Massachusetts Institute of Technology, Cambridge, MA 02139, USA*
[2]*TAPIR, Walter Burke Institute for Theoretical Physics, California Institute of Technology, Mailcode 350-17, Pasadena, CA 91125, USA*

Accepted 2020 June 22. Received 2020 June 22; in original form 2020 May 5

ABSTRACT

Compact white dwarf (WD) binaries are important sources for space-based gravitational-wave (GW) observatories, and an increasing number of them are being identified by surveys like Extremely Low Mass (ELM) and Zwicky Transient Facility (ZTF). We study the effects of non-linear dynamical tides in such binaries. We focus on the global three-mode parametric instability and show that it has a much lower threshold energy than the local wave-breaking condition studied previously. By integrating networks of coupled modes, we calculate the tidal dissipation rate as a function of orbital period. We construct phenomenological models that match these numerical results and use them to evaluate the spin and luminosity evolution of a WD binary. While in linear theory the WD's spin frequency can lock to the orbital frequency, we find that such a lock cannot be maintained when non-linear effects are taken into account. Instead, as the orbit decays, the spin and orbit go in and out of synchronization. Each time they go out of synchronization, there is a brief but significant dip in the tidal heating rate. While most WDs in compact binaries should have luminosities that are similar to previous traveling-wave estimates, a few per cent should be about 10 times dimmer because they reside in heating rate dips. This offers a potential explanation for the low luminosity of the CO WD in J0651. Lastly, we consider the impact of tides on the GW signal and show that the *Laser Interferometer Space Antenna* (*LISA*) and *TianGO* can constrain the WD's moment of inertia to better than 1 per cent for centi-Hz systems.

Key words: gravitational waves – instabilities – (*stars*:) binaries (*including multiple*): close – stars: oscillations – white dwarfs.

1 INTRODUCTION

As binary white dwarfs (WDs) with short orbital periods inspiral due to the emission of gravitational waves (GWs), they can evolve into a variety of interesting systems, including AM CVn stars (Nelemans et al. 2001), R Cor Bor stars (Clayton 2012), and rapidly rotating magnetic WDs (Ferrario, de Martino & Gänsicke 2015). Merging WDs may also explode as Type Ia supernovae (Iben & Tutukov 1984; Webbink 1984; Toonen, Nelemans & Portegies Zwart 2012; Polin, Nugent & Kasen 2019b) or in other types of luminous thermonuclear events (Shen et al. 2018; Polin, Nugent & Kasen 2019a). Compact WD binaries emit GWs with frequencies of ≈1–100 mHz, which makes them prominent sources for proposed space-based GW observatories such as the *Laser Interferometer Space Antenna* (*LISA*; Amaro-Seoane et al. 2017), *TianQin* (Luo et al. 2016), and *TianGO* (Kuns et al. 2019).

The tidal interaction between the binary components spins them up and heats their interiors. As they inspiral, the tide becomes progressively stronger and eventually their spin frequency nearly equals the orbital frequency. However, they never become perfectly synchronous because of the continual GW-induced orbital decay. The degree of spin asynchronicity affects the tidal heating rate and luminosity of the WDs (Iben, Tutukov & Fedorova 1998; Fuller & Lai 2012a, 2013; Piro 2019) and the outcome of their potential merger (Raskin et al. 2012; Dan et al. 2014; Fenn, Plewa & Gawryszczak 2016).

The dominant mechanism of tidal dissipation is most likely the excitation of internal gravity waves, either in the form of standing waves (i.e. g-modes; Fuller & Lai 2011; Burkart et al. 2013), or traveling waves (Fuller & Lai 2012a,b, 2013, 2014). As we will show, for orbital periods between approximately 10 and 150 min, which describe many of the observed WD binaries, the resonant g-modes excited by the tide have such large amplitudes that they cannot be considered small, linear perturbations to the background star. On the other hand, the amplitudes are not so large that the modes break due to strong non-linearities. The tidal dynamics and dissipation in this intermediate, weakly non-linear regime are complicated and depend on details of the non-linear coupling between g-modes driven directly by the tide and the sea of secondary modes they excite.

In this paper, we apply the weakly non-linear tidal formalism developed in Weinberg et al. (2012) to study tides in WD binaries. Our study fills the gap between those that assume the excited modes are linear standing waves (e.g. Fuller & Lai 2011; Burkart et al. 2013) and those that assume they break and form strongly non-linear traveling waves (Fuller & Lai 2012a,b, 2013, 2014). In Section 2, we present the background WD model we use throughout much of our analysis. In Section 3, we describe the mode coupling and tidal driving equations that govern the mode dynamics, and in Section 4, we describe our numerical method for solving these equations. In Section 5, we present our solutions of the mode dynamics and show how tidal dissipation and synchronization varies with orbital period in the weakly non-linear regime. We also compare our results with the previous studies that assumed the tide was either linear or strongly non-linear. In Section 6, we describe the observable electromagnetic

★ E-mail: hangyu@caltech.edu

© 2020 The Author(s)
Published by Oxford University Press on behalf of the Royal Astronomical Society

Downloaded from https://academic.oup.com/mnras/article/496/4/5482/5863236 by California Institute of Technology user on 22 October 2020

Table 1. The mass M, radius R, effective temperature $T_{\rm eff}$, and moment of inertia $I_{\rm WD}$ of our WD model. We will often express results in terms of the primary's natural units of energy $E_0 \equiv GM^2/R = 1.10 \times 10^{50}$ erg and frequency $\omega_0 \equiv \sqrt{GM/R^3} = 0.346$ rad s^{-1}.

M	R	$T_{\rm eff}$	$I_{\rm WD}$
0.6 $M_\odot$	8.75×10^8 cm	9000 K	$0.257MR^2$

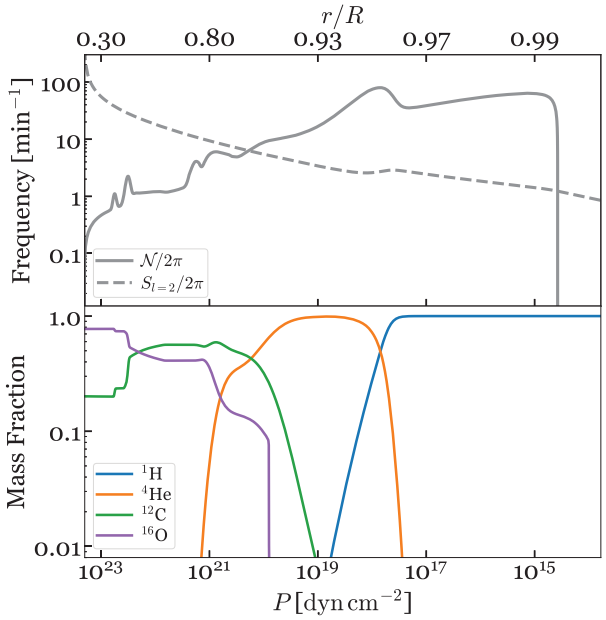

Figure 1. Propagation diagram (top panel) and composition profile (bottom panel) of our WD model from the centre to the surface. Note that we have oriented the bottom x-axis such that the radius increases to the right.

and GW signatures of the tidal interaction, including the tidal heating luminosities, GW phase shifts, and projected constraints on the WD moment of inertia. In Section 7, we summarize our key results and conclude.

2 BACKGROUND MODEL

We use MESA (version 10398; Paxton et al. 2011, 2013, 2015, 2018) to construct a WD model, whose key parameters are summarized in Table 1. To construct this model, we adopt parameters similar to those used by Timmes et al. (2018). Specifically, we start with a pre-main-sequence star with an initial mass of 2.8 $M_\odot$ and metallicity $Z = 0.02$ and let it evolve to a CO WD with mass $M = 0.6\,M_\odot$ and effective temperature $T_{\rm eff} = 9000$ K. We include element diffusion, semiconvection, and thermohaline mixing throughout the evolution. We use GYRE (Townsend & Teitler 2013; Townsend, Goldstein & Zweibel 2018) to compute the model's eigenmodes and construct our mode networks.

In the upper panel of Fig. 1, we show the propagation diagram of our WD model. The solid line is the buoyancy frequency $\mathcal{N}$, where

$$\mathcal{N}^2 = g^2 \left(\frac{1}{c_{\rm e}^2} - \frac{1}{c_{\rm s}^2} \right), \tag{1}$$

$c_{\rm e}^2 = {\rm d}P/{\rm d}\rho$ is the equilibrium sound speed squared, $c_{\rm s}^2 = \Gamma_1 P/\rho$ is the adiabatic sound speed squared, and Γ_1 is the adiabatic index. All other quantities have their usual meaning. The dashed line is the Lamb frequency S_l for $l = 2$, where

$$S_l^2 = \frac{l(l+1)c_{\rm s}^2}{r^2}. \tag{2}$$

For the short-wavelength g-modes that comprise the dynamical tide, the square of the radial wavenumber,

$$k_r^2 = \frac{\omega^2}{c_{\rm s}^2} \left(\frac{S_l^2}{\omega^2} - 1 \right) \left(\frac{\mathcal{N}^2}{\omega^2} - 1 \right), \tag{3}$$

where ω is the angular eigenfrequency of the mode. A g-mode propagates where $k_r^2 > 0$, i.e. in regions where $\omega < \mathcal{N}$ and $\omega < S_l$, and is evanescent where $k_r^2 < 0$.

The lower panel of Fig. 1 shows the composition profile of our model. As is typical of stars supported by degeneracy pressure, the buoyancy is due largely to composition gradients, with peaks in $\mathcal{N}$ associated with sharp transitions in the internal composition.

3 FORMALISM

3.1 Equation of motion

Consider a primary star of mass M and a secondary star of mass M' and choose a coordinate system whose origin is at the centre of the primary and corotates with it. We assume that the orbit is circular and that the spin angular momentum of the primary is aligned with the orbital angular momentum. For simplicity, we do not account for the effect of rotation on the mode dynamics except through the Doppler shift of the tidal driving frequency. The equation of motion governing the Lagrangian displacement field $\boldsymbol{\xi}(\boldsymbol{r}, t)$ of a perturbed fluid element at location $\boldsymbol{r}$ at time t is then (see e.g. Schenk et al. 2002; Weinberg et al. 2012, hereafter WAQB12)

$$\rho \ddot{\boldsymbol{\xi}} = \boldsymbol{f}_1[\boldsymbol{\xi}] + \boldsymbol{f}_2[\boldsymbol{\xi}, \boldsymbol{\xi}] + \rho \boldsymbol{a}_{\rm tide}, \tag{4}$$

where $\boldsymbol{f}_1$ and $\boldsymbol{f}_2$ represent the linear and leading-order non-linear internal restoring forces, and

$$\boldsymbol{a}_{\rm tide} = -\nabla U - (\boldsymbol{\xi} \cdot \nabla) \nabla U \tag{5}$$

is the tidal acceleration. The tidal potential can be expanded as

$$U(\boldsymbol{r}, t) = -\sum_{l \geq 2, m} W_{lm} \frac{GM'}{D(t)} \left[\frac{r}{D(t)} \right]^l Y_{lm}(\theta, \phi)\, {\rm e}^{-{\rm i}m(\Omega_{\rm orb} - \Omega_{\rm s})t}, \tag{6}$$

where Y_{lm} is the spherical harmonic function, and D, $\Omega_{\rm orb}$, and $\Omega_{\rm s}$ are the orbital separation, the orbital angular frequency, and the spin frequency of the primary, respectively. We focus on the leading-order quadrupolar ($l = 2$) tide, whose non-vanishing W_{lm} coefficients are $W_{2\pm2} = \sqrt{3\pi/10}$ and $W_{20} = -\sqrt{\pi/5}$. It is useful to define

$$\epsilon = \left(\frac{M'}{M} \right) \left(\frac{R}{D} \right)^3 = \left(\frac{y}{1+y} \right) \left(\frac{\Omega_{\rm orb}}{\omega_0} \right)^2, \tag{7}$$

where $y = M'/M$ is the mass ratio. The quantity ϵ characterizes the overall tidal strength and will be useful when we want to distinguish the system's dependence on the tidal strength from its dependence on the driving frequency $2(\Omega_{\rm orb} - \Omega_{\rm s})$.

In order to solve equation (4), we expand the six-dimensional phase-space vector as

$$\begin{bmatrix} \boldsymbol{\xi}(\boldsymbol{r}, t) \\ \dot{\boldsymbol{\xi}}(\boldsymbol{r}, t) \end{bmatrix} = \sum_a q_a(t) \begin{bmatrix} \boldsymbol{\xi}_a(\boldsymbol{r}) \\ -{\rm i}\omega_a \boldsymbol{\xi}_a(\boldsymbol{r}) \end{bmatrix}, \tag{8}$$

where $q_a(t)$, ω_a, and $\boldsymbol{\xi}_a(\boldsymbol{r})$, are the amplitude, frequency, and displacement of an eigenmode labelled by subscript a. The frequency

Downloaded from https://academic.oup.com/mnras/article/496/4/5482/5863236 by California Institute of Technology user on 22 October 2020

and displacement are found by solving the linear, homogeneous equation

$$\boldsymbol{f}_1[\boldsymbol{\xi}_a] = -\rho\omega_a^2\boldsymbol{\xi}_a, \tag{9}$$

which we normalize as

$$2\omega_a^2\int \mathrm{d}^3 r\,\rho\boldsymbol{\xi}_a^*\cdot\boldsymbol{\xi}_b = \frac{GM^2}{R}\delta_{ab} \equiv E_0\delta_{ab}. \tag{10}$$

Each eigenmode has a unique set of three quantum numbers: its angular degree l_a, azimuthal order m_a, and radial order n_a. The summation in equation (8) runs over all mode quantum numbers and both signs of eigenfrequency in order to include each mode and its complex conjugate.[1] Using the orthogonality of the eigenmodes, equation (4) can now be expressed as a set of evolution equations for the mode amplitudes:

$$\dot{q}_a + (\mathrm{i}\omega_a + \gamma_a)q_a = \mathrm{i}\omega_a\left[U_a + \sum_b U_{ab}^* q_b^* + \sum_{bc}\kappa_{abc}q_b^* q_c^*\right], \tag{11}$$

where

$$U_a(t) = -\frac{1}{E_0}\int \mathrm{d}^3 r\,\rho\,\boldsymbol{\xi}_a^*\cdot\nabla U, \tag{12}$$

$$U_{ab}(t) = -\frac{1}{E_0}\int \mathrm{d}^3 r\,\rho\,\boldsymbol{\xi}_a\cdot\left(\boldsymbol{\xi}_b\cdot\nabla\right)\nabla U, \tag{13}$$

$$\kappa_{abc} = \frac{1}{E_0}\int \mathrm{d}^3 r\,\boldsymbol{\xi}_a\cdot\boldsymbol{f}_2\left[\boldsymbol{\xi}_b,\boldsymbol{\xi}_c\right]. \tag{14}$$

The linear and non-linear tidal coefficients U_a and U_{ab} characterize the strength of the coupling of modes to the tide, and the three-mode coupling coefficient κ_{abc} characterizes the strength of the coupling of modes to each other.

We further simplify equation (11) by noting that the three-mode coupling involving the equilibrium tide cancels significantly with the non-linear tide (i.e. $\sum_{c\in\mathrm{eq}}\kappa_{abc}q_c^* \simeq -U_{ab}$; WAQB12). We therefore ignore U_{ab} and the equilibrium tide and focus on the dynamical tide.[2] The latter is dominated by the linear driving of the most-resonant $l_a = |m_a| = 2$ modes, for which $|\Delta_a/\omega_a| \ll 1$, where $\Delta_a = \omega - \omega_a$ is the linear detuning and $\omega = 2(\Omega_{\rm orb} - \Omega_{\rm s})$ is the linear driving frequency. We refer to such linearly resonant modes as parent modes. By contrast, the other modes in our networks (the daughters, granddaughters, etc.) are primarily excited through three-mode parametric resonances rather than direct driving by the tide since they have large $|\Delta_a|$ and smaller U_a than the parents (since they have larger n_a and l_a; see equations 23 and 30). In our mode network calculations, we therefore solve a reduced set of amplitude equations in which the parent modes $\{a\}$ satisfy

$$\dot{q}_a + (\mathrm{i}\omega_a + \gamma_a)q_a = \mathrm{i}\omega_a U_a + \mathrm{i}\omega_a\sum_{bc}\kappa_{abc}q_b^* q_c^*, \tag{15}$$

[1]If the amplitudes q_{a+} and q_{a-} correspond to eigenfrequencies ω_a and $-\omega_a$, respectively, then the reality of $\boldsymbol{\xi}$ requires $q_{a+} = q_{a-}^*$, where the asterisk denotes complex conjugation.

[2]We note that the non-linear driving by equilibrium tide might be unstable depending on the residual coupling. Roughly, the growth rate for the equilibrium-tide-driven instability is $\Gamma_{\rm nl}^{(\rm eq)} \sim \epsilon\kappa_{abc}^{(\rm eq)}(\Omega_{\rm orb} - \Omega_{\rm s})$. If the residual coupling $\kappa_{abc}^{(\rm eq)} \sim 1$ after accounting for the cancellation with U_{ab}, then we have $\Gamma_{\rm nl}^{(\rm eq)} \sim 10^{-8}$ s at $P_{\rm orb} = 50$ min. This, while smaller than the non-linear growth rate of the dynamical tide (equation 47), could be greater than the damping rate of the resonant $l = 2$ modes at the same period. We defer the study of this effect to future work.

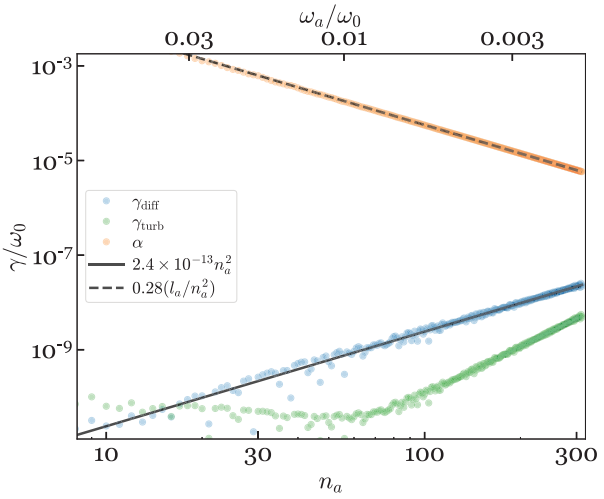

Figure 2. Linear damping rate of $l_a = 2$ modes. The blue and green circles represent the respective contributions of radiative diffusion $\gamma_{\rm diff}$ and convective turbulence $\gamma_{\rm turb}$. The orange circles are the inverse group traveling time α of each mode (see Section 3.5). The solid and dashed black lines show the Wentzel–Kramers–Brillouin (WKB) scaling relations (equations 21 and 42).

and the daughter modes $\{b, c\}$ satisfy

$$\dot{q}_b + (\mathrm{i}\omega_b + \gamma_b)q_b = \mathrm{i}\omega_b\sum_{ac}\kappa_{abc}q_a^* q_c^*, \tag{16}$$

and similarly for the granddaughters, great-granddaughters, etc.

The energy of a mode $E_a(t)$ is related to its amplitude by

$$E_a(t) = q_a^*(t)q_a(t)E_0. \tag{17}$$

This neglects the energy in the three-mode coupling,

$$\frac{1}{3}\sum_{b,c}\kappa_{abc}q_a q_b q_c + \text{c.c.}, \tag{18}$$

where c.c. stands for complex conjugate. As we show in Section 3.4, this energy is much less than $\sum_a E_a$ and, therefore, we will use equation (17) to represent the mode energy.

3.2 Power-law relations for the coefficients

In Appendix A, we describe our calculations of γ_a, U_a, and κ_{abc} in detail. For the tidal synchronization problem, we are mostly interested in binaries with orbital periods in the range $P_{\rm orb} = [10, 100]$ min, which corresponds to $l_a = 2$ parent modes with radial orders in the range $n_a \simeq [10, 100]$ (see equation 20). For such high-order modes, we find that the coefficients follow simple power-law relations in n_a and l_a.

We find that the eigenfrequencies of our WD model are approximately given by

$$\omega_a \simeq 0.28\frac{l_a}{n_a}\omega_0 = 0.098\frac{l_a}{n_a}\,\mathrm{rad\,s^{-1}}, \tag{19}$$

i.e. the mode periods are given by

$$P_a = \frac{2\pi}{\omega_a} \simeq 1.1\frac{n_a}{l_a}\,\mathrm{min}, \tag{20}$$

where $\omega_0 = \sqrt{GM/R^3}$ is the dynamical frequency of the WD.

In Fig. 2, we show the linear dissipation rates γ_a. The dissipation is dominated by electron conduction and radiative diffusion and for

Downloaded from https://academic.oup.com/mnras/article/496/4/5482/5863236 by California Institute of Technology user on 22 October 2020

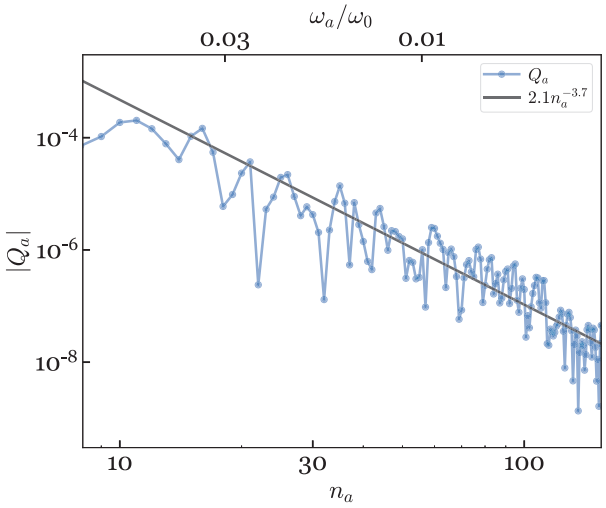

Figure 3. Linear tidal overlap Q_a (blue circles). The black line is the fit given by equation (23).

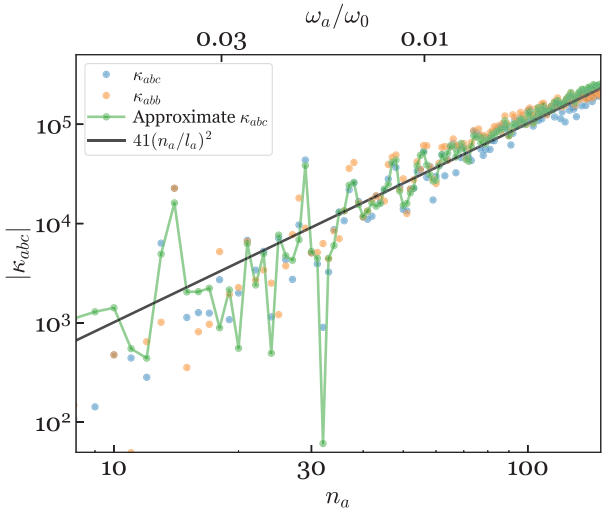

Figure 4. Three-mode-coupling coefficient κ_{abc} as a function of the parent mode's radial order. The blue circles are the coupling computed with daughter pairs that have the smallest frequency detuning with respect to the parent mode, and the orange circles further restrict it to self-coupled daughters ($b = c$). The green circles connected with solid lines use the approximate expression for the coupling coefficient integrand given by equation (A18). Note that for a given parent mode a, its κ_{abc} for different daughter pairs satisfying the selection rules are all approximately equal as long as $|n_b - n_c| \lesssim n_a$.

$n_a \gg l_a$ (as is true of all modes in our networks) is approximately given by

$$\gamma_a \simeq 2.4 \times 10^{-13} n_a^2 \omega_0 = 8.4 \times 10^{-14} n_a^2 \, \mathrm{s}^{-1}. \tag{21}$$

By comparison, the dissipation due to turbulent convective damping (green dots) is much smaller for the modes we are interested in (see Appendix A for details).

From equations (6) and (12), we can write the linear tide coefficient as

$$U_a = W_{lm} Q_a \left(\frac{M'}{M}\right) \left(\frac{R}{D}\right)^{l+1} \mathrm{e}^{-\mathrm{i}m(\Omega_{\rm orb} - \Omega_{\rm s})t}, \tag{22}$$

where the overlap integral

$$Q_a = \frac{1}{MR^l} \int \mathrm{d}^3 r \rho \boldsymbol{\xi}^* \cdot \nabla \left(r^l Y_{lm}\right) \simeq 2.1 n_a^{-3.7} \delta_{l_a l} \delta_{m_a m}. \tag{23}$$

In Fig. 3, we show Q_a, calculated using the method described in Appendix A3, and the numerical fit above. Note that the overlap is non-zero only if $l_a = l$ and $m_a = m$.

In Fig. 4, we show the three-mode coupling coefficients as a function of the parent mode's radial order n_a. For high-order modes, we find

$$\kappa_{abc} \simeq 41 \left(\frac{T}{0.18}\right) \left(\frac{n_a}{l_a}\right)^2, \tag{24}$$

where a is the parent mode. Here T is an angular integral that depends only on each mode's angular quantum numbers and vanishes if the modes do not satisfy the angular selection rules: (i) $|l_b - l_c| \le l_a \le l_b + l_c$, (ii) $l_a + l_b + l_c$ is even, and (iii) $m_a + m_b + m_c = 0$. Otherwise, it is of order unity for the typical triplets that we consider, e.g. $T \simeq 0.18$ for $l_a = l_b = l_c = 2$ and $(m_a, m_b, m_c) = (2, -2, 0)$. In addition to these angular selection rules, the modes couple significantly only if their radial orders satisfy $|n_b - n_c| \lesssim n_a$ (Wu & Goldreich 2001; WAQB12).

3.3 Non-linear instability threshold

In the absence of non-linear interactions, a mode driven by the linear tide has an energy

$$\frac{E_{a,\rm lin}}{E_0} = \frac{\omega_a^2}{\Delta_a^2 + \gamma_a^2} U_a^2, \tag{25}$$

where $\Delta_a = \omega - \omega_a$ and $\omega = m(\Omega_{\rm orb} - \Omega_{\rm s})$. In linear theory, the parent's energy and dissipation rate are smallest when the parent is half-way between resonances, i.e. when the detuning is at a maximum $|\Delta_a| = |\partial\omega_a/\partial n_a|/2 \simeq \omega_a/2n_a$ ($\gg \gamma_a$ for the periods of interest). The linear energy of a parent half-way between resonances is

$$\frac{\overline{E}_{a,\rm lin}}{E_0} = 7.9 \times 10^{-18} \left(\frac{2y}{1+y}\right)^2 \left(\frac{P_{\rm orb}}{50\,\mathrm{min}}\right)^{-9.3}, \tag{26}$$

assuming a non-rotating WD such that $P_a \simeq P_{\rm orb}/2$.

Now consider a simple three-mode system consisting of a parent mode driven by the tide coupled to a resonant daughter pair. If $\overline{E}_{a,\rm lin} > E_{\rm th}$ the parent is unstable even at maximum Δ_a, where the energy threshold (see e.g. WAQB12; Essick & Weinberg 2016, hereafter EW16)

$$\frac{E_{\rm th}}{E_0} = \frac{1}{4\kappa_{abc}^2} \left(\frac{\gamma_b \gamma_c}{\omega_b \omega_c}\right) \left[1 + \left(\frac{\Delta_{bc}}{\gamma_b + \gamma_c}\right)^2\right], \tag{27}$$

with $\Delta_{bc} = \omega + \omega_b + \omega_c$ the non-linear detuning. Note that if $\omega > 0$, we have $\omega_b, \omega_c < 0$ according to our sign convention.

In Fig. 5, we show $\overline{E}_{a,\rm lin}$ (dotted line) and the minimum $E_{\rm th}$ from a numerical search of daughter pairs (black crosses) assuming a non-rotating WD. We also show an analytic estimate of the minimum $E_{\rm th}$ (blue line), whose calculation we describe below. We see that for $P_{\rm orb} \lesssim 150$ min, even maximally detuned parent modes are parametrically unstable. In fact, since $\overline{E}_{a,\rm lin} \gg E_{\rm th}$ over much of this range, we will see that a single parent excites many unstable daughter pairs.

The daughter pairs that minimize $E_{\rm th}$ are those that satisfy the κ_{abc} selection rules, have $|n_b - n_c| < n_a$, and non-linear detunings $\Delta_{bc} \approx \gamma_b + \gamma_c$ since they minimize the sum in quadrature in the brackets of equation (27); see also EW16. We can obtain an analytic estimate of the minimum $E_{\rm th}$ by using the scaling relations given above and an estimate for the minimum Δ_{bc}. Following the argument given by Wu & Goldreich (2001), we obtain an estimate for the minimum Δ_{bc}

Downloaded from https://academic.oup.com/mnras/article/496/4/5482/5863236 by California Institute of Technology user on 22 October 2020

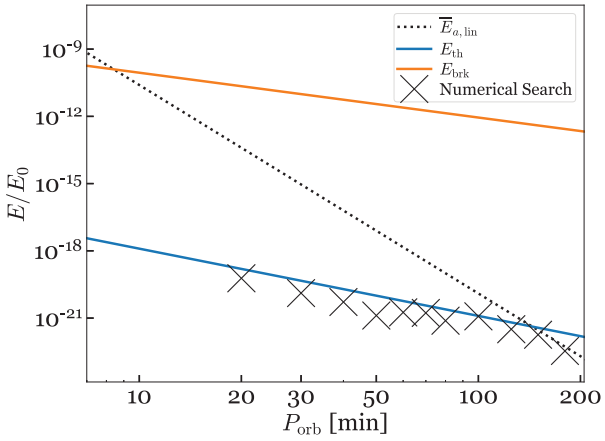

Figure 5. Linear energy $\overline{E}_{a,\rm lin}$ for a parent half-way between adjacent resonance peaks (equation 26; dotted black line), the non-linear threshold energy $E_{\rm th}$ based on the analytic scaling relations (equation 29; blue line), and the wave-breaking energy $E_{\rm brk}$ (equation 44; orange line) as a function of orbital period assuming a non-rotating WD. The black crosses show the minimum $E_{\rm th}$ obtained from a numerical search for daughter pairs.

by noting that for a fixed parent mode a, there are $\sim n_a^2$ daughter pairs satisfying $|n_b - n_c| \lesssim n_a$ at fixed l_b and l_c. As we allow the angular degree l_b and l_c to vary, we obtain an extra factor of $l_b l_a$ of mode pairs that satisfy the condition $|l_b - l_c| < l_a < l_b + l_c$. The eigenfrequencies of these potential daughter modes span a range of order $n_a|\partial\omega_b/\partial n_b| \simeq n_a\omega_b/n_b$. Therefore, the typical minimum three-mode detuning assuming a non-rotating WD is of order[3]

$$\Delta_{bc} \approx \frac{1}{l_b l_a n_a^2}\frac{n_a\omega_b}{n_b} \simeq \frac{0.07 l_a \omega_0}{l_b^2 n_a^3}, \tag{28}$$

where in the second approximation we first eliminated n_b in terms of (ω_b, l_b) using equation (19) and then assumed that $|\omega_b| \simeq \omega_a/2$. The factor of 0.07 is from a fit to our numerical search for daughter pairs that minimize $E_{\rm th}$. By using the scaling relations in Section 3.2 and equation (28) and setting $\Delta_{bc} \simeq \gamma_b + \gamma_c$, it follows that the minimum threshold energy

$$\frac{E_{\rm th}}{E_0} \simeq 1.0\times10^{-20}\left(\frac{0.18}{T}\right)^2\left(\frac{P_{\rm orb}}{50\,{\rm min}}\right)^{-3}, \tag{29}$$

where this assumes a non-rotating WD and $P_a = P_{\rm orb}/2$. As Fig. 5 shows, this $E_{\rm th}$ estimate is in good agreement with that from the numerical search for daughter pairs. The daughters that minimize $E_{\rm th}$ typically have

$$l_b \simeq 6.0\left(\frac{P_{\rm orb}}{50\,{\rm min}}\right)^{-5/4} \text{ and } n_b \simeq 281\left(\frac{P_{\rm orb}}{50\,{\rm min}}\right)^{-1/4}. \tag{30}$$

3.4 Energy and angular momentum transfer

In this section, we derive the tidal power $\dot{E}_{\rm tide}$ and the tidal torque $\tau_{\rm tide}$ in the inertial frame. We define the torque to be from the orbit to the WD and when $\tau_{\rm tide} > 0$ the tide spins up the WD. Given the interaction Hamiltonian

$$H_{\rm int} = -2E_0\sum_{\omega_a>0}\left(q_a^* U_a + q_a U_a^*\right), \tag{31}$$

the tidal torque acting on the WD is

$$\begin{aligned}\tau_{\rm tide} &= \frac{\partial H_{\rm int}}{\partial\Phi} \simeq -4\sum_{\omega_a>0}{\rm Re}\left[q_a^*\frac{\partial U_a}{\partial\Phi}\right]E_0\\ &= -4\sum_{\omega_a>0} m_a {\rm Im}\left[q_a^* U_a\right]E_0,\end{aligned} \tag{32}$$

where a factor of 2 arises from the sum over modes and their complex conjugate and another because we restricted the sum to positive frequencies, and the last equality follows because $\partial U_a/\partial\Phi = -{\rm i}mU_a$. Note that we dropped the term $\propto U_{ab}$ in the interaction Hamiltonian because only the linearly resonant parents have a significant direct coupling to the tide (Section 3.1).

The associated tidal power, assuming a circular orbit, is given by

$$\dot{E}_{\rm tide} = \Omega_{\rm orb}\tau_{\rm tide}. \tag{33}$$

In general, this will power a combination of mode energy, tidal heating, and WD spin energy. However, as we illustrate in Section 5.1 (see e.g. Figs 7 and 8), in steady state the time-averaged total mode energy is approximately constant and $\sum_a \dot{E}_a \simeq \sum_a\left(\dot{q}_a^* q_a + q_a^*\dot{q}_a\right)E_0 \simeq 0$. Using equation (15) we thus have, in a time-averaged sense,

$$\sum_a \omega_a {\rm Im}\left[q_a^* U_a\right] \simeq -\sum_b \gamma_b q_b^* q_b. \tag{34}$$

The summation on the left-hand side is only over parent modes since only they feel a strong, direct driving by the tide (Section 3), whereas on the right-hand side it is over all modes from all generations. We also dropped the three-mode dissipation terms as they contribute little to the total dissipation.[4]

For the most-resonant parent modes with $\omega_a \geq 0$ and $l_a = 2$, the azimuthal order $m_a = m = 2$ and $\omega_a \simeq \omega = m(\Omega_{\rm orb} - \Omega_{\rm s})$. We can therefore relate the tidal torque and power to the total dissipation rate inside the star, $\dot{E}_{\rm diss}$, as

$$\tau_{\rm tide} = \frac{m}{\omega}\dot{E}_{\rm diss}, \tag{35}$$

$$\dot{E}_{\rm tide} = \frac{\Omega_{\rm orb}}{(\Omega_{\rm orb} - \Omega_{\rm s})}\dot{E}_{\rm diss}, \tag{36}$$

where

$$\dot{E}_{\rm diss} = 4\sum_{\omega_b>0}\gamma_b q_b^* q_b E_0 \simeq 4\sum_{\omega_b>0}\gamma_b E_b. \tag{37}$$

If we assume that the WD rotates with uniform angular velocity $\Omega_{\rm s}$, then the tidal torque spins it up at a rate

$$\dot{\Omega}_{\rm s} = \frac{\tau_{\rm tide}}{I_{\rm WD}}, \tag{38}$$

and the orbital frequency changes at a rate

$$\dot{\Omega}_{\rm orb} = \dot{\Omega}_{\rm orb,gw} + \frac{3\tau_{\rm tide}}{\mu D^2}, \tag{39}$$

where the GW-induced orbital decay rate

$$\dot{\Omega}_{\rm orb,gw} = \frac{96}{5}\left(\frac{G\mathcal{M}_{\rm c}}{c^3}\right)^{5/3}\Omega_{\rm orb}^{11/3}. \tag{40}$$

Here μ is the reduced mass and $\mathcal{M}_{\rm c} = y^{3/5}(1+y)^{-1/5}M$ is the chirp mass. In our study, we obtain $\dot{E}_{\rm diss}$ from our mode network

[3]For a rotating WD, the detuning is smaller by yet another factor of l_b because the degeneracy between different combinations of m_b and m_c is lifted (i.e. rotational splitting).

[4]The three-mode coupling contributes $-2\sum_{abc}\gamma_a\kappa_{abc}{\rm Re}[q_a q_b q_c]$ to the dissipation, which arises from the non-linear piece in the total mode energy (equation 18). Since $|\sum_{abc}\kappa_{abc}q_a q_b q_c| \ll \sum_a E_a$ (see last paragraph of this section), the non-linear dissipation is much smaller than the lower order contribution $\sum_a\gamma_a E_a$.

Downloaded from https://academic.oup.com/mnras/article/496/4/5482/5863236 by California Institute of Technology user on 22 October 2020

simulations according to equation (37) and thereby determine $\tau_{\rm tide}$, $\dot{\Omega}_{\rm s}$, and $\dot{\Omega}_{\rm orb}$.[5]

Our large non-linear networks display complicated dynamics. None the less, some insights can be gained by considering the non-linear equilibrium of simple three-mode systems (WAQB12; EW16). For such a system, the parent mode's saturation is $E_{a,\rm s} = E_{\rm th}$ and for $\overline{E}_{a,\rm lin} \gg E_{a,\rm s}$, the daughter mode's equilibrium is

$$\frac{E_{b,\rm s}}{E_0} \simeq \sqrt{\frac{\gamma_c \omega_b}{\gamma_b \omega_c}} \left| \frac{U_a}{2\kappa_{abc}} \right| \simeq 6.7 \times 10^{-16} \left(\frac{2y}{1+y} \right) \left(\frac{P_{\rm orb}}{50\,{\rm min}} \right)^{-7.7}. \quad (41)$$

Comparing equations (29) and (41), we see that $E_{b,\rm s} \simeq E_{c,\rm s} \gg E_{a,\rm s}$. As a result, the leading order drive to the granddaughters will be via daughter–granddaughter three-mode coupling rather than parent–granddaughter coupling at higher non-linear orders. We therefore include multiple generations in our networks but only account for three-mode coupling between adjacent generations.[6]

Energy is stored not only in each individual mode ($\propto E_a$) but also in the three-mode couplings ($\propto {\rm Re}[\kappa_{abc} q_a q_b q_c]$; see equation 18). However, the latter makes a negligible contribution to the total energy at saturation. We can easily see this for a three-mode system, since at saturation the total non-linear energy is $\sim \kappa_{abc}\sqrt{E_{a,\rm s}} E_{b,\rm s} \ll E_{b,\rm s}$. To see roughly why this also holds for our large mode networks, note that at saturation the non-linear forces approximately balance the linear forces. By equation (11), this implies $|\sum_{bc} \kappa_{abc} q_b^* q_c^*|$ approximately equals $|U_a|$ for parent modes and $(\gamma/\omega_a)|q_a|$ for the other modes. Since both are $\ll |q_a|$, it follows that $|\sum_{bc} \kappa_{abc} q_a q_b q_c| \ll E_a$ and therefore the non-linear energy is a small contribution to the total energy.

3.5 Standing waves versus traveling waves

The relations above and our mode network calculations assume that the modes are all standing waves. In order to be a standing wave, a mode's linear damping time must be longer than its group travel time through the propagation cavity (which here spans much of the WD radius; see Fig. 1), $T_a = 2\int {\rm d}r\, v_{\rm grp}^{-1} = 2\int {\rm d}r ({\rm d}\omega_a/{\rm d}k_r)^{-1}$, where $v_{\rm grp}$ is the mode's group velocity (BQAW13; Ivanov, Papaloizou & Chernov 2013). Otherwise, it is a traveling wave.[7] Defining the inverse group travel time $\alpha_a = 2\pi/T_a$, we find

$$\alpha_a \simeq 0.28 \frac{l_a}{n_a^2} \omega_0 = 0.097 \frac{l_a}{n_a^2}\ {\rm rad\,s^{-1}}. \quad (42)$$

In Fig. 2, we compare α_a to the linear damping rate of modes. We find that the standing wave condition $\gamma_a < \alpha_a$ is satisfied for

$$n_a \lesssim 1200 \left(\frac{l_a}{2} \right)^{1/4}, \ {\rm i.e.}\ P_{\rm orb} \lesssim 1320 \left(\frac{l_a}{2} \right)^{-3/4}\ {\rm min}, \quad (43)$$

which is true of all the modes in our networks.

[5]Alternatively, we can compute $\tau_{\rm tide}$ by taking the time average of equation (32) in steady state. Although we verified that the two methods yield consistent results, in practice we find that ${\rm Im}[q_a^* U_a]$ of individual parents is much more oscillatory than $\sum_b \gamma_b E_b$ and thus equation (37) provides a more numerically accurate estimate of the torque.

[6]Four-mode coupling can be important for the *p*–*g* instability (Venumadhav, Zimmerman & Hirata 2014; Weinberg 2016). However, that is a non-resonant instability, whereas here we focus on the resonant parametric instability.

[7]Note that this condition is equivalent to the linear damping rate γ_a being smaller than the frequency difference between two adjacent g-modes, $|\partial\omega_a/\partial n_a| \simeq \omega_a/n_a$. One can show that under the Wentzel–Kramers–Brillouin (WKB) approximation, $\alpha_a = \omega_a/n_a$. This can also be seen by comparing the numerical values of equations (19) and (42).

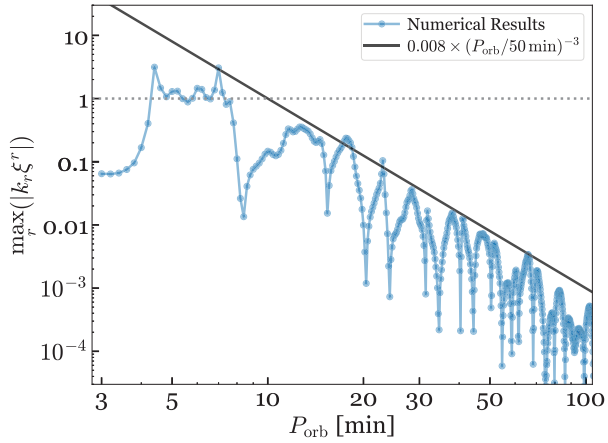

Figure 6. Maximum local shear $|k_r\xi_r|$ from the traveling-wave solution for a non-rotating WD with $T_{\rm eff} = 9000$ K.

Another necessary condition for standing wave is that the shear $|{\rm d}\xi_r/{\rm d}r| \simeq |k_r\xi_r|$ be everywhere less than unity, where $\xi_r Y_{lm}$ is the radial component of the physical Lagrangian displacement $\boldsymbol{\xi}$. If a g-mode's shear exceeds unity, it is strongly non-linear and overturns the local stratification and breaks (see e.g. Goodman & Dickson 1998; Ogilvie & Lin 2007; Barker 2011).

Fuller & Lai (2012a, hereafter FL12) and Burkart et al. (2013, hereafter BQAW13) use this local wave-breaking condition to address the onset of non-linear tidal effects in WD binaries. They show that at sufficiently short orbital periods, the tide excites internal gravity waves that are initially linear deep within the WD but become non-linear and break as they approach the stellar surface.[8]

We first evaluate the wave-breaking condition *assuming a standing wave*, i.e. a g-mode. Using the approach described in Appendix A1, we find that a g-mode's shear exceeds unity if its energy exceeds (see equation A4)

$$\frac{E_{\rm brk}}{E_0} = 3.6 \times 10^{-12} \left(\frac{P_{\rm orb}}{50\,{\rm min}} \right)^{-2}. \quad (44)$$

In Fig. 5, we show $E_{\rm brk}$ as a function of $P_{\rm orb}$. We find that $\overline{E}_{a,\rm lin}$ first exceeds $E_{\rm brk}$ at $P_{\rm orb} \simeq 10$ min. Moreover, even highly resonant parent modes are unlikely to break before $P_{\rm orb} \simeq 10$ min. That is because the parent is parametrically unstable ($E_{a,\rm lin} > E_{\rm th}$) out to $P_{\rm orb} \approx 150$ min (Fig. 5) and excites secondary modes that prevent it from reaching the wave-breaking limit (see Section 5.1).

We now evaluate the wave-breaking condition *assuming a traveling wave* rather than a standing wave. Specifically, we use the approach described in FL12 (see Appendix C for a brief synopsis) to find the traveling-wave solution of the linear inhomogeneous tidal equations (equations C1–C3). Just as the standing wave assumption is valid only if $\max|k_r\xi_r| < 1$, the traveling-wave assumption is valid only if $\max|k_r\xi_r| > 1$. In Fig. 6, we show $\max|k_r\xi_r|$ computed under the traveling-wave assumption for a non-rotating WD with $T_{\rm eff} = 9000$ K. We find that the upper envelope of the shear $\propto P_{\rm orb}^{-3}$ (which we explain in Appendix C) and reaches unity at $P_{\rm orb} \simeq 10$ min, consistent with the results assuming a standing wave.

The weakly non-linear regime of this study therefore spans a large range of orbital periods ($10 \lesssim P_{\rm orb}/{\rm min} \lesssim 150$). Evaluating the global,

[8]It is interesting to note that whereas the local wave breaking occurs at the surface, the global three-mode coupling happens mostly in the core region; see Appendix A4 and Fig. 4. This is different from the case of solar models (WAQB12).

Downloaded from https://academic.oup.com/mnras/article/496/4/5482/5863236 by California Institute of Technology user on 22 October 2020

multimode dynamics in this regime is essential for understanding the impact of tidal dissipation on WD binaries.

Our analysis assumes that all modes, not just the parent, are standing waves and thus below the wave-breaking threshold. Since $E_{\rm th} \propto \omega^3$ while $E_{\rm brk} \propto \omega^2$, higher generation (i.e. lower frequency) modes have even smaller ratios of $E_{\rm th}$ to $E_{\rm brk}$ than the parent. Thus, the excited daughters, granddaughters, etc. will likely become parametrically unstable and saturate before breaking (see also appendix F in EW16). In practice, because we truncate our networks at the fifth generation and include only the most-resonant pairs for each generation (since including more modes does not significantly increase the calculated $\dot{E}_{\rm diss}$; see Section 5.2), some high generation modes in our network can have shears that momentarily exceed unity. However, at any given time these represent only a very small fraction of the excited modes and thus they are unlikely to modify the overall dynamics and dissipation.

It is also worth noting that the shear can be a sensitive function of the WD temperature. For example, in Appendix A1, we show that for $T_{\rm eff} = 18\,000$ K the maximum shear is about an order of magnitude larger than for 9000 K. On the other hand, this is compensated by the tidal synchronization that decreases the driving frequency (see Section 5.4 and Appendix C). The orbital period where the dynamical tide transitions from weakly to strongly non-linear is therefore still $\approx$10 min when the effects of both temperature and synchronization are taken into account.

4 NUMERICAL IMPLEMENTATION

The modes in our networks oscillate near their eigenfrequencies and have small linear detunings Δ_a (parents) or non-linear detunings Δ_{bc} (daughters, granddaughters, etc.). We can therefore factor out the fast oscillations by transforming coordinates to $c_a = q_a \exp({\rm i}\omega_a t)$, similar to the approach of previous mode network studies (Brink, Teukolsky & Wasserman 2005; EW16). The parent mode amplitude equation (15) is then

$$\dot{c}_a + \gamma_a c_a = {\rm i}\omega_a |U_a| {\rm e}^{-{\rm i}\Delta_a t} + {\rm i}\omega_a \sum_{bc} \kappa_{abc} c_b^* c_c^* {\rm e}^{{\rm i}\Delta'_{bc} t}, \tag{45}$$

and similarly for the other modes, where $\Delta'_{bc} = \omega_a + \omega_b + \omega_c$. We initialize our networks by starting each mode at its linear tidal energy and a random phase. We implemented the calculations in PYTHON and used the NUMBA package (Lam, Pitrou & Seibert 2015) to enhance the computational performance.

Initially, the amplitudes of the unstable daughters will grow exponentially at a characteristic rate (see WAQB12),

$$\Gamma_{\rm nl} \simeq \omega_a \kappa_{abc} \sqrt{\frac{E_a}{E_0}}. \tag{46}$$

This allows us to define a characteristic non-linear growth time-scale,

$$T_{\rm nl} \equiv \frac{1}{\Gamma_{\rm nl}} \sim 0.12 \left(\frac{P_{\rm orb}}{50\,{\rm min}}\right)^{3.7} {\rm yr}, \tag{47}$$

where the numerical value is for a parent mode at an initial energy $\overline{E}_{a,{\rm lin}}$.

We find that the mode networks saturate and reach a non-linear equilibrium over a few non-linear growth times $T_{\rm nl}$. This is much shorter than the GW-induced orbital decay time-scale,

$$T_{\rm gw} = \frac{\Omega_{\rm orb}}{\dot{\Omega}_{\rm orb,gw}} = 4.8 \times 10^7 \left(\frac{P_{\rm orb}}{50\,{\rm min}}\right)^{8/3} {\rm yr}, \tag{48}$$

where the numerical value assumes a typical WD binary with $M = M' = 0.6\,{\rm M}_\odot$. The time-scale $T_{\rm nl}$ is also shorter than the time it takes for the GW orbital decay to change the three-mode detuning Δ_{bc} by an amount $(\gamma_b + \gamma_c) \simeq 2\gamma_b$ (see Section 3.3),

$$T_{\rm det} = \frac{\gamma_b}{\dot{\Omega}_{\rm orb,gw}} \simeq 150 \left(\frac{P_{\rm orb}}{50\,{\rm min}}\right)^{19/6} {\rm yr}. \tag{49}$$

Therefore, the particular parametrically unstable pairs that are most resonant and thus have the lowest $E_{\rm th}$ do not change on a time-scale of a few $T_{\rm nl}$. We therefore only construct our mode networks once for each $P_{\rm orb}$ we consider.

In order to construct our mode networks, we search for the daughters, granddaughters, etc. with the lowest threshold energies. Numerically, we find that a network's total energy dissipation rate $\dot{E}_{\rm diss}$ converges once we include five mode generations constructed as follows. The first generation (parents) includes the two most linearly resonant modes. The second generation (daughters) includes the three lowest threshold daughter pairs of each parent. Since the two parent modes both oscillate at the tidal driving frequency, they usually have the same pair of most-resonant daughter modes and thus the second generation typically has six modes instead of 12. The third through fifth generations include the single lowest threshold pair of each mode from the previous generation. A typical network consists of 92 modes, with (2, 6, 12, 24, and 48) modes in each generation (since modes sometimes appear in more than one pair, some networks have slightly fewer than 92 modes). We find that increasing the number of modes and generations does not significantly change the computed $\dot{E}_{\rm diss}$ (see Section 5.2).

A collective instability can occur if daughters form large sets of mutually coupled pairs (WAQB12). Collectively unstable daughters initially grow much more rapidly than the isolated pairs described above. However, in our problem the collective instability threshold $E_{\rm th,\,col}$ is higher than the isolated pair instability threshold $E_{\rm th}$. EW16 found that the parents, whose linear energy might be well above $E_{\rm th,\,col}$, reach a non-linear equilibrium at an energy below $E_{\rm th,\,col}$ due to their coupling to isolated pairs. As a result, they found that the collective pairs eventually decay away and thus do not enhance the net dissipation in the system. We expect similar dynamics here and therefore do not include collectively unstable pairs in our networks.

5 RESULTS

Having described the formalism and numerical methods in Sections 3 and 4, we now describe the results of our coupled mode network simulations. In Section 5.1, we show representative examples of the mode dynamics on short time-scales. In Section 5.2, we show how the total energy dissipation rate depends on orbital period over a wide range of orbital separations. In Section 5.3, we describe semi-analytic models that accurately capture the scalings found in the network simulations. In all three sections, we assume a non-rotating WD in an equal mass binary. In Section 5.4, we consider a rotating WD and study the impact of the tide on the spin evolution and synchronization of the binary.

5.1 Mode dynamics on short time-scales

In the top panel of Fig. 7, we show a zoomed-in view of the energy $E_a(t)$ of each mode in our network over a duration of approximately one non-linear growth time-scales $T_{\rm nl}$ (equation 47) at an orbital period near $P_{\rm orb} \simeq 60$ min. The top panel of Fig. 8 is similar except at $P_{\rm orb} \simeq 30$ min. In both figures, the precise periods are chosen in order that the most-resonant parent mode has a detuning $|\Delta_a| = \omega_a/3n_a$, which is somewhat far from a resonance peak ($|\Delta_a| = \omega_a/2n_a$ half-way between adjacent resonance peaks). The solid grey line in

Downloaded from https://academic.oup.com/mnras/article/496/4/5482/5863236 by California Institute of Technology user on 22 October 2020

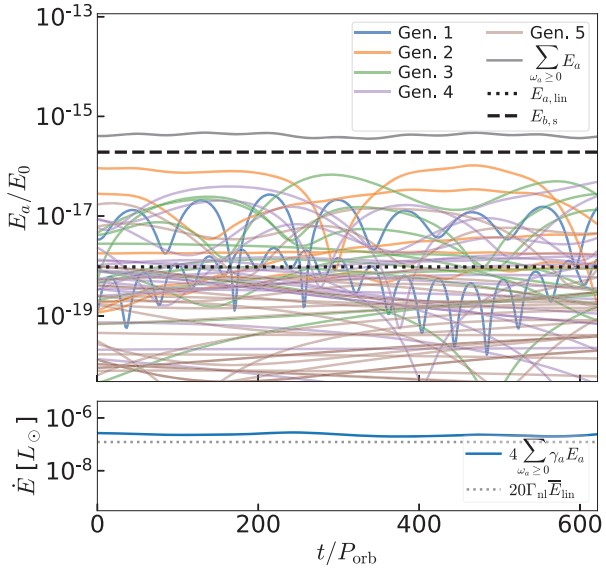

Figure 7. Mode energy (upper panel) and total energy dissipation rate (lower panel) as a function of time at an orbital period $P_{\rm orb}$=59.46 min. At this period, the most-resonant parent has a detuning $|\Delta_a| = \omega_a/3n_a$. We include five generations of modes and in the upper panel label the first (i.e. the parent) to the fifth generation of modes with blue, orange, green, purple, and brown lines, respectively. The grey solid line is the total mode energy. For comparison, we also show the mode energy according to linear theory (equation 25; black dotted line) and the three-mode equilibrium energy of the daughter modes (black dashed line) estimated using equation (41). In the lower panel, the blue solid line is the numerically computed total dissipation rate $\dot{E}_{\rm diss}$ and the grey dotted line is 20 times the product of the maximally detuned parent mode energy $\overline{E}_{a,\rm lin}$ and the corresponding three-mode growth rate (equation 46).

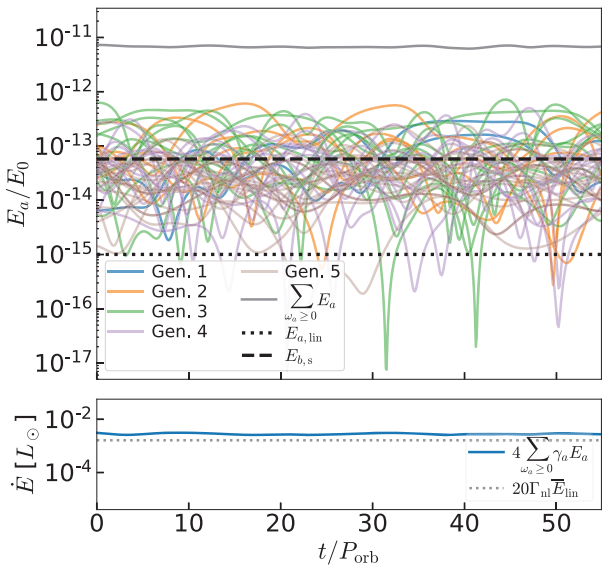

Figure 8. Same as Fig. 7 but at $P_{\rm orb}$=28.48 min.

each figure shows the total mode energy $E_{\rm tot} = \sum_a E_a$. Although an individual mode's energy can vary by orders of magnitude over time, we find that over duration of a few $T_{\rm nl}$, the system settles into a quasi-equilibrium state with $E_{\rm tot} \approx$ constant. Thus, there is a balance between the time-averaged tidal power driving the parents and the

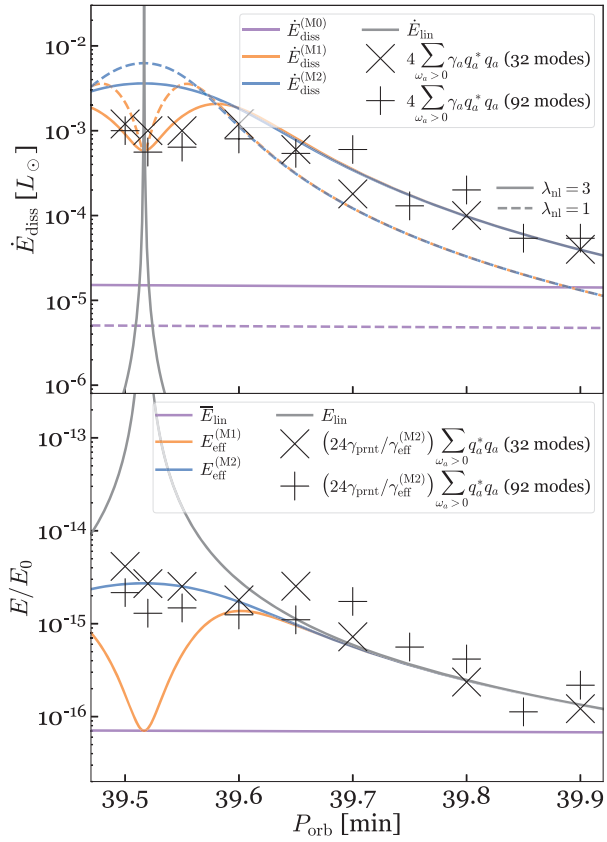

Figure 9. Top panel: tidal dissipation rate $\dot{E}_{\rm diss}$ as a function of orbital period near $P_{\rm orb} = 40$ min assuming a non-rotating WD. The period range shown spans $\simeq$0.5 min, which corresponds to half of the separation between two adjacent linear resonances. We show $\dot{E}_{\rm diss}$ computed with the standard 92-mode network (+ symbols) and a 32-mode network ($\times$ symbols). The coloured lines show $\dot{E}_{\rm diss}$ according to linear theory (grey line) and models M0, M1, and M2 (purple, orange, and blue) for $\lambda_{\rm nl} = 1$ (dashed lines) and $\lambda_{\rm nl} = 3$ (solid lines); we see that the latter value provides the best fit to the numerical results. Bottom panel: similar to the top panel but showing energy rather than $\dot{E}_{\rm diss}$. We show the total mode energy $E_{\rm tot}$ in the two networks, the parent linear energy $E_{\rm lin}$ (grey line), the maximally detuned parent linear energy $\overline{E}_{a,\rm lin}$ (purple line), and the effective energies $E_{\rm eff}$ of models M1 and M2 (orange and blue lines). Note that $E_{\rm tot}$ has been multiplied by a factor of $24\gamma_a/\gamma_{\rm eff}^{\rm (M2)} \ll 1$, where γ_a is the linear damping rate of the parent mode. We do this in order to be able to show it on the same scale as $E_{\rm lin}$ and $E_{\rm eff}$.

net thermal dissipation from mode damping. We also find that $E_{\rm tot} \gg E_{\rm lin}$, where $E_{\rm lin}$ is the total energy according to linear theory (dotted black line; equation 25).

We note that there is no energy hierarchy in the mode generation. In fact, modes from different generations alternatively dominate the system's energy in a limit-cycle-like (or even chaotic) manner with a variation time-scale shorter than $T_{\rm nl}$.

In the bottom panels of Figs 7 and 8, we show the numerically computed energy dissipation rate $\dot{E}_{\rm diss} = 4\sum_{\omega_a>0}\gamma_a E_a$ on short time-scales. Similar to $E_{\rm tot}$, we find that $\dot{E}_{\rm diss} \approx$ constant.

5.2 Energy dissipation as a function of orbital period

We now use the numerical results at individual $P_{\rm orb}$ to determine the time-averaged non-linear dissipation as a function of orbital separation.

Downloaded from https://academic.oup.com/mnras/article/496/4/5482/5863236 by California Institute of Technology user on 22 October 2020

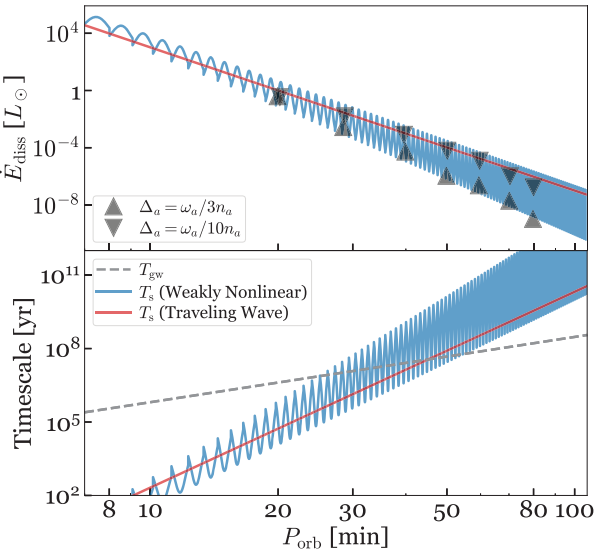

Figure 10. Top panel: energy dissipation rate $\dot{E}_{\rm diss}$ as a function of orbital period. The up (down) triangles show results of the 92-mode network at $P_{\rm orb}$ where the parent has a relatively large (small) detuning $|\Delta_a| = \omega/3n_a$ ($\omega/10n_a$). The blue line shows results of the weakly non-linear model M2 and the red line shows results of the traveling-wave model. Bottom panel: the spin-up time-scale $T_{\rm s}$ for model M2 (blue line) and the traveling-wave model (red line). The dashed line is the GW-induced orbital decay time-scale $T_{\rm gw}$. In both panels we assume a non-rotating WD and use $\lambda_{\rm nl} = 3$ when evaluating M2.

In the upper panel of Fig. 9, we show $\dot{E}_{\rm diss}$ over a narrow range of orbital period near $P_{\rm orb} \simeq 40$ min (corresponding to resonance of the $n_a = 37$ parent mode). The range is chosen to span half the distance between two adjacent linear resonances. We find that $\dot{E}_{\rm diss}$ is many orders of magnitude larger than the linear energy dissipation rate $\dot{E}_{\rm lin}$ (solid grey line) except when extremely near the resonance peak. Although the non-linear dissipation is much less sensitive to distance from resonance than the linear dissipation, it does still vary significantly with Δ_a. In going from on-resonance to half-way between resonance, $\dot{E}_{\rm diss}$ decreases by a factor of $\simeq$10 at $P_{\rm orb} \simeq 40$ min. As we show below, it is even more sensitive to Δ_a at larger $P_{\rm orb}$.

In Fig. 9, we show results for our standard 92-mode network with (2, 6, 12, 24, and 48) modes in each generation, and a 32-mode network with (2, 2, 4, 8, and 16) modes in each generation (see Section 4). The $\dot{E}_{\rm diss}$ of each agree to within a factor of about 2. We also verified that adding the next two most-resonant parent modes ($n_a = 36$ and 39) does not affect the energy dissipation by more than $\mathcal{O}$(10 per cent). From these experiments we performed, we conclude that our 92-mode network is sufficiently large to adequately capture the full non-linear dissipation.

In Fig. 10, we show $\dot{E}_{\rm diss}$ over a wide range of $P_{\rm orb}$. The triangles are the results from a series of mode network simulations, with the upward (downward) triangles corresponding to $P_{\rm orb}$ when the most-resonant parent has a relatively large (small) detuning $|\Delta_a| = \omega_a/3n_a$ ($\omega_a/10n_a$). We find that the difference in $\dot{E}_{\rm diss}$ between peaks and trough decreases considerably with decreasing $P_{\rm orb}$; the difference is a factor of $\sim 10^3$ at $P_{\rm orb} \simeq 80$ min, while it is only a factor of $\sim$30 at $P_{\rm orb} \simeq 20$ min.

From the numerical results, we see that the dissipation scales approximately as $\dot{E}_{\rm diss} \propto P_{\rm orb}^{-13}$ when the detuning is large. Since the typical linear damping of the modes in the network scales approximately[9] as $\gamma_a \propto P_{\rm orb}^{-2}$, the total mode energy at large detuning $E_{\rm tot} \propto P_{\rm orb}^{-11}$. As a result, although the simple three-mode daughter equilibrium energy $E_{b,\rm s} \propto P_{\rm orb}^{-7.7}$ (equation 41) roughly equals $E_{\rm tot}$ at $P_{\rm orb} \approx 60$ min (Fig. 7), it is significantly smaller than $E_{\rm tot}$ at $P_{\rm orb} \approx 30$ min (Fig. 8).

5.3 Semi-analytic models of the dissipation rate

Since the mode network integrations are computationally expensive, it is useful to have a semi-analytic model calibrated to the numerical results that can provide an estimate of $\dot{E}_{\rm diss}$ over the full range of $P_{\rm orb}$. Here we consider models in which the energy dissipation rate is approximated as

$$\dot{E}_{\rm diss} = 4\gamma_{\rm eff} E_{\rm eff}, \tag{50}$$

where $E_{\rm eff}$ is an effective energy and $\gamma_{\rm eff}$ is an energy-dependent effective damping rate. The factor of 4 accounts for the two frequency signs and the fact that $\gamma_{\rm eff}$ is the amplitude, rather than energy, damping rate.

5.3.1 Model 0

In Model 0 (M0), our simplest model, we assume that

$$\begin{aligned} \gamma_{\rm eff}^{\rm (M0)} &= \Gamma_{\rm nl} = \lambda_{\rm nl}\omega_a\kappa_{abc}\sqrt{\frac{\overline{E}_{a,\rm lin}}{E_0}}, \\ E_{\rm eff}^{\rm (M0)} &= \overline{E}_{a,\rm lin}, \end{aligned} \tag{51}$$

which implies

$$\dot{E}_{\rm diss}^{\rm (M0)} = 4\gamma_{\rm eff}^{\rm (M0)} E_{\rm eff}^{\rm (M0)} \propto \left(\frac{2y}{1+y}\right)^3 \Omega_{\rm orb}^6 \omega_a^{7.0}, \tag{52}$$

where $\Gamma_{\rm nl}$ is given by equation (47) evaluated at a parent energy $E_a = \overline{E}_{a,\rm lin}$, modes b, c are the fastest growing daughter pair, and $\lambda_{\rm nl}$ is a dimensionless constant whose value is determined by fitting to the numerical results. We separated our $\dot{E}_{\rm diss}^{\rm (M0)}$ expression into the part that depends on $\Omega_{\rm orb}$ and the part that depends on the eigenfrequency ω_a [which is further related to the driving frequency $\omega = m(\Omega_{\rm orb} - \Omega_{\rm s}) \simeq \omega_a$]. The $\Omega_{\rm orb}$ dependence arises from terms that scale with the overall tidal amplitude ϵ (equation 7), while the ω_a dependence arises from terms that depend on the internal structure of the resonant parent modes (e.g. Q_a, γ_a, κ_{abc}, etc.). Separating the expression for energy dissipation rates in this way will be useful when we consider a rotating WD and tidal synchronization in Section 5.4.

M0 is similar to one proposed in Kumar & Goodman (1996) who studied non-linear mode damping in tidal capture binaries. In their analysis, the binary is on a highly eccentric orbit and the parent is excited from essentially zero energy to a linear energy $E_{a,\rm lin}$ during pericentre passage (using the method of Press & Teukolsky 1977). They argue that $\dot{E}_{\rm diss} \approx 4\Gamma_{\rm nl} E_{a,\rm lin}$ because that is the maximum rate at which the fastest growing daughter pair can drain energy from an undriven parent that has an initial energy $E_{a,\rm lin}$.

In the bottom panels of Figs 7 and 8, we compare M0 to the network simulations. Although M0 can match the simulations at both $P_{\rm orb} \simeq$ 30 and 60 min, the agreement is only good at the large detuning $\Delta_a = \omega_a/3n_a$ assumed in both figures. Since $\dot{E}_{\rm diss}^{\rm (M0)}$ is independent of Δ_a, it cannot account for the significant variation of $\dot{E}_{\rm diss}$ with Δ_a seen in

[9]This ignores the fact that the dissipation at different instants may be dominated by modes from different generations. Therefore, at a given $P_{\rm orb}$, the linear damping among different modes can vary by factors of $\mathcal{O}$(10).

Downloaded from https://academic.oup.com/mnras/article/496/4/5482/5863236 by California Institute of Technology user on 22 October 2020

the numerical simulations (see Figs 9 and 10). This failure is perhaps not surprising since here, unlike the highly eccentric orbit of the tidal capture problem, there is a continuous, Δ_a-dependent interaction between the parent's tidal driving and non-linear damping.

5.3.2 Model 1

In order to construct models that depend on Δ_a, we next consider effective energies with Lorentzian profiles of the form

$$\frac{E_{\rm eff}}{E_0} = \frac{\omega_a^2}{\Delta_a^2 + \gamma_{\rm eff}^2} U_a^2. \tag{53}$$

This is similar to the expression for linear energy (equation 25) except that the linear damping rate γ_a is replaced by the effective damping rate $\gamma_{\rm eff}$.[10]

Since M0 gives a reasonable approximation to the dissipation rate when Δ_a is large, we construct models by starting from M0 and using an iterative approach to improve upon it. Specifically, starting with the maximally detuned linear energy of the parent $\overline{E}_{a,\rm lin}$, we first define the 0th-order expressions:

$$\begin{aligned}
\gamma_{\rm eff}^{(0)} &= \lambda_{\rm nl}\omega_a\kappa_{abc}\sqrt{\frac{\overline{E}_{a,\rm lin}}{E_0}}, \\
\frac{E_{\rm eff}^{(0)}}{E_0} &= \frac{\omega_a^2}{\Delta_a^2 + \left[\gamma_{\rm eff}^{(0)}\right]^2} U_a^2.
\end{aligned} \tag{54}$$

We then use these to evaluate the next order expressions, which define our Model 1 (M1),

$$\begin{aligned}
\gamma_{\rm eff}^{(\rm M1)} &= \lambda_{\rm nl}\omega_a\kappa_{abc}\sqrt{\frac{E_{\rm eff}^{(0)}}{E_0}}, \\
\frac{E_{\rm eff}^{(\rm M1)}}{E_0} &= \frac{\omega_a^2}{\Delta_a^2 + \left[\gamma_{\rm eff}^{(\rm M1)}\right]^2} U_a^2.
\end{aligned} \tag{55}$$

Note that $E_{\rm eff}^{(\rm M1)}$ is *not* the total energy stored in the non-linear network (see the upper panels of Figs 7 and 8). Instead, the total energy is greater than $E_{\rm eff}^{(\rm M1)}$ by a factor of $\mathcal{O}(\gamma_{\rm eff}/\gamma_a) \gg 1$, as shown in the lower panel of Fig. 9.

5.3.3 Model 2

An alternative and perhaps more natural choice of energy at which to evaluate $\gamma_{\rm eff}$ is $E_{\rm eff}$ itself. This choice defines our Model 2 (M2), namely

$$\begin{aligned}
\gamma_{\rm eff}^{(\rm M2)} &= \lambda_{\rm nl}\omega_a\kappa_{abc}\sqrt{\frac{E_{\rm eff}^{(\rm M2)}}{E_0}}, \\
\frac{E_{\rm eff}^{(\rm M2)}}{E_0} &= \frac{\omega_a^2}{\Delta_a^2 + \left[\gamma_{\rm eff}^{(\rm M2)}\right]^2} U_a^2 \\
&= \frac{-\Delta_a^2 + \sqrt{\Delta_a^4 + 4\lambda_{\rm nl}^2\omega_a^4\kappa_{abc}^2 U_a^2}}{2\lambda_{\rm nl}^2\omega_a^2\kappa_{abc}^2}.
\end{aligned} \tag{56}$$

[10]This model should only be applied when $\gamma_{\rm eff}$ is smaller than the frequency spacing between two adjacent g-modes, $|\partial\omega_a/\partial n_a| \simeq \omega_a/n_a$, as is the case here. This ensures the parent mode is a standing wave (see also Section 3.5) and the dynamics are well characterized by the most-resonant parent mode alone.

The second equality in the effective energy expression follows by solving the quadratic equation for $E_{\rm eff}$. Note that if we keep performing the iteration process we used in M1, it will eventually converge to M2.

It will be useful to have the M2 scaling relations for the effective energy and the energy dissipation rate when the parent mode is exactly on resonance. We find

$$\frac{E_{\rm eff}^{(\rm M2)}}{E_0}(\Delta_a{=}0) = \frac{U_a}{\lambda_{\rm nl}\kappa_{abc}} \propto \left(\frac{2y}{1+y}\right)\Omega_{\rm orb}^2\omega_a^{5.7}, \tag{57}$$

$$\dot{E}_{\rm diss}^{(\rm M2)}(\Delta_a{=}0) \propto \left(\frac{2y}{1+y}\right)^{3/2}\Omega_{\rm orb}^3\omega_a^{7.5}. \tag{58}$$

Note that the resonant effective energy scales with the orbital frequency as $\Omega_{\rm orb}^2$, whereas the linear tidal energy scales as $\Omega_{\rm orb}^4$. The difference is due to the fact that the non-linear damping term $\gamma_{\rm eff}$ is itself a function of tidal energy, whereas the linear damping γ_a is independent of $\Omega_{\rm orb}$. We will use equation (58) in Section 5.4 to address the possibility of resonant locking (as studied in BQAW13 for linear tides) in the weakly non-linear tide regime.

5.3.4 Traveling-wave limit

In Section 3.5, we showed that in the traveling-wave regime ($P_{\rm orb} \lesssim 10$ min), the internal gravity waves excited in the core reach such large amplitudes that they become strongly non-linear and break near the stellar surface. Although the focus of our study is instead weakly non-linear mode coupling in the standing wave regime ($10 \lesssim P_{\rm orb}/{\rm min} \lesssim 150$), it is none the less instructive to compare the predictions of the two regimes as if one or the other applied at all $P_{\rm orb}$.

The tidal evolution in the traveling-wave regime was studied in detail by FL12 (see also BQAW13). In Appendix C, we review key aspects of the traveling-wave solution and show that it gives an energy dissipation

$$\dot{E}_{\rm diss}^{(\rm tw)} \simeq \hat{f}\omega E_0\left(\frac{y}{1+y}\right)^2\left(\frac{\Omega_{\rm orb}}{\omega_0}\right)^4\left(\frac{\omega}{\omega_0}\right)^5 \propto \Omega_{\rm orb}^4\omega^6, \tag{59}$$

where $\omega = 2(\Omega_{\rm orb} - \Omega_{\rm s})$ is the frequency at which the wave is forced (there are no resonances) and $\hat{f}$ is a dimensionless quantity that characterizes the overall strength of the dissipation. Based on our WD model, we find $\hat{f} \simeq 20$ (see Fig. C1), which agrees well with the value obtained by FL12 for a similar model. The above equation is related to the tidal energy transfer rate (see equation 42 in FL12) by $\dot{E}_{\rm tide}^{(\rm tw)} = (\Omega_{\rm orb}/\omega)\,\dot{E}_{\rm diss}^{(\rm tw)}$.

The models adopted by FL12 and BQAW13 are effectively linear models since $\dot{E}_{\rm diss} \propto \epsilon^2 \propto \Omega_{\rm orb}^4$. In our weakly non-linear models, by contrast, $\gamma_{\rm eff}$ is itself a function of ϵ and thus the dissipation does not scale as $\Omega_{\rm orb}^4$ (see e.g. equation 58). We will show in Section 5.4 that this can result in a substantially different spin evolution.

5.3.5 Comparison of tidal dissipation models

In the upper panel of Fig. 9, we show that M1 and M2 provide a good fit to the mode network simulations for $\lambda_{\rm nl} \simeq 3$. Moreover, they provide a much better fit than M0, especially at small $|\Delta_a|$. Although near exact resonance M1 provides a better fit than M2, we show in Appendix B that the tidal synchronization and heating are similar in the two models. We therefore adopt M2 as our fiducial model, as its analytic form is simpler than M1's.

In the top panel of Fig. 10, we show $\dot{E}_{\rm diss}$ of M2 over a wide range of $P_{\rm orb}$. We see that it agrees well with the network

Downloaded from https://academic.oup.com/mnras/article/496/4/5482/5863236 by California Institute of Technology user on 22 October 2020

simulations both in terms of its overall $P_{\rm orb}$ scaling and the high-frequency oscillations with Δ_a (modulo the slight overestimate near the resonance peaks, as noted above). It also helps explain why the oscillations decrease in amplitude at smaller $P_{\rm orb}$; namely, $\gamma_{\rm eff}$ increases and becomes comparable to the maximum detuning, which smears out the resonance peaks.

In Fig. 10, we also show the dissipation $\dot{E}^{\rm (tw)}_{\rm diss}$ if we treat the dynamical tide as a traveling wave at large $P_{\rm orb}$ (even though it is a standing wave). We find that the traveling-wave solution appears to trace the upper envelope of the weakly non-linear solution. However, this is merely a coincidence. Indeed, comparing equations (58) and (59) we see that they only have similar scaling when the spin rate is fixed at zero so that $\omega_a \simeq 2\Omega_{\rm orb}$. When we consider the tidal synchronization problem, they in fact have qualitatively different behaviours.

5.4 Tidal synchronization and heating

We now study the tidal synchronization and heating of the WD by using the calculation of $\dot{E}_{\rm diss}$ to solve for the tidal torque $\tau_{\rm tide}$ (equation 35) and thereby determine $\dot{\Omega}_{\rm s}$ and $\dot{\Omega}_{\rm orb}$ (equations 38 and 39). We use $\dot{E}_{\rm diss}$ as given by model M2 with $\lambda_{\rm nl} = 3$ since it provides a useful analytic form that agrees well with the numerical results (Section 5.3).

In the top panel of Fig. 11, we show the evolution of $\Omega_{\rm s}$ and the asynchronicity $\Omega_{\rm asyn} \equiv \Omega_{\rm orb} - \Omega_{\rm s}$ as a function of $P_{\rm orb}$. We initialize the frequencies at $\Omega_{\rm orb} = 2\pi/(240\,{\rm min})$ and $\Omega_{\rm s} = \Omega_{\rm orb}/30$, although we find that the synchronization calculation is insensitive to the initial conditions as long as both frequencies are initially small. Initially both $\Omega_{\rm s}$ and $\Omega_{\rm asyn}$ increase as the orbit decays but at a critical orbital period $P_{\rm c} \simeq 50$ min the spin-up has an inflection point and $\Omega_{\rm asyn}$ becomes nearly constant. This is because at $P_{\rm c}$, the spin-up time-scale,

$$T_{\rm s} = \frac{\Omega_{\rm orb}}{\dot{\Omega}_{\rm s}}, \tag{60}$$

first becomes smaller than the orbital decay time-scale $T_{\rm gw} = \Omega_{\rm orb}/\dot{\Omega}_{\rm orb,gw}$ (equation 48), as shown in the bottom panel of Fig. 10. By evaluating $\dot{E}_{\rm diss}$ using model M2 at a resonance $\Delta_a = 0$ (see equation 58), where the dissipation has a local maximum and thus $T_{\rm s}$ has a local minimum, we find that the condition $T_{\rm s} = T_{\rm gw}$ is first satisfied at

$$P_{\rm c} = 55\left(\frac{\lambda_{\rm nl}}{3}\right)^{-0.09}\ {\rm min}. \tag{61}$$

Although model M2 slightly overestimates $\dot{E}_{\rm diss}$ at resonances (see Section 5.3), this estimate of $P_{\rm c}$ is robust owing to the weak dependence on $\lambda_{\rm nl}$.

For $P_{\rm orb} < P_{\rm c}$, the spin frequency $\Omega_{\rm s}$ continues to increase as the orbit decays. Meanwhile, the asynchronicity $\Omega_{\rm asyn}$ is nearly constant, although importantly it continues to increase, albeit slowly. This continual increase implies that the system never acquires a resonance lock. In a resonance lock, the tidal torque causes the tidal forcing frequency $|\omega| = 2\Omega_{\rm asyn}$ to remain constant even as the orbit shrinks (Witte & Savonije 1999). BQAW13 found that resonance locks should occur universally in WD binaries, whether the parent is a standing wave or a traveling wave. However, their study did not account for non-linear mode coupling, which we find prevents resonance locks from forming in the standing-wave regime ($P_{\rm orb} \gtrsim 10$ min; Section 3.5). This is because $\dot{\Omega}_{\rm s} \propto \dot{E}_{\rm diss}$ and based on model M2, $\dot{E}_{\rm diss} \propto \Omega^3_{\rm orb}\omega_a^{7.5}$ at perfect resonance $\Delta_a = 0$ (equation 58). Thus, if $\omega_a \simeq \omega$ remains at a constant value near $4\pi/P_{\rm c}$

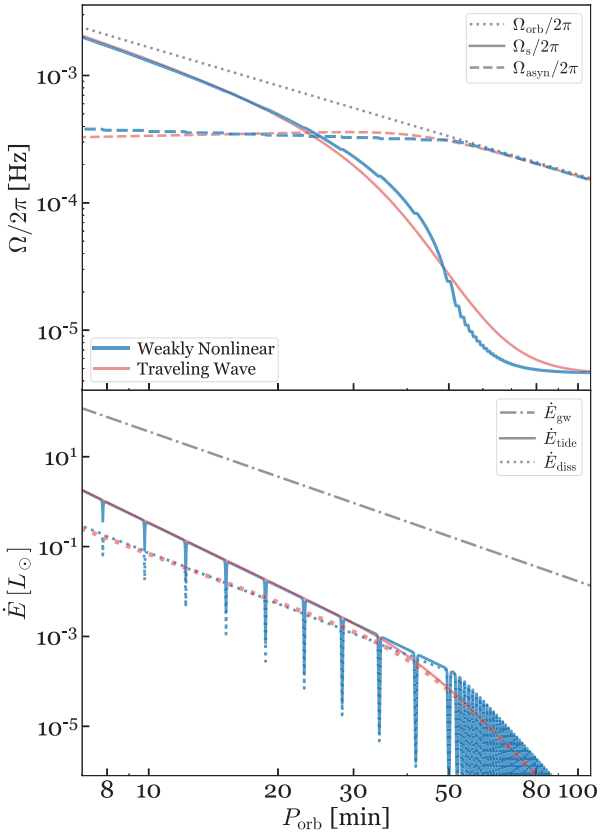

Figure 11. Top panel: spin frequency $\Omega_{\rm s}$ (solid lines), asynchronicity $\Omega_{\rm asyn} = \Omega_{\rm orb} - \Omega_{\rm s}$ (dashed lines), and orbital frequency $\Omega_{\rm orb}$ (dotted lines) as a function of orbital period $P_{\rm orb}$. Bottom panel: tidal power $\dot{E}_{\rm tide}$ (solid line), tidal dissipation rate inside the star $\dot{E}_{\rm diss}$ (dotted line), and GW power $\dot{E}_{\rm gw}$ (dash–dotted line) as a function of $P_{\rm orb}$. In both panels, the blue lines correspond to the weakly non-linear model M2 (assuming $\lambda_{\rm nl} = 3$) and the red lines correspond to the traveling-wave model.

for $P_{\rm orb} < P_{\rm c}$, we have $T_{\rm s} \propto \Omega^{-2}_{\rm orb}$ and since $T_{\rm gw} \propto \Omega^{-8/3}_{\rm orb}$ even the maximal tidal torque at $\Delta_a = 0$ is insufficient to maintain a resonance lock as $\Omega_{\rm orb}$ increases.

To better illustrate why resonance locks do not form, in Fig. 12 we show a zoomed-in view of the spin evolution over three consecutive resonances. The top panel shows $\Omega_{\rm asyn}$ and the bottom panel shows $1 - T_{\rm gw}/T_{\rm s}$. We see that at resonances (shaded regions), the tidal torque is nearly strong enough to keep $\Omega_{\rm asyn}$ constant and a lock almost forms. However, the torque is not quite sufficient to maintain synchronization as the orbit decays (as evidenced by the weaker $\Omega_{\rm orb}$ scaling of $T_{\rm s} \propto \Omega^{-2}_{\rm orb}$ than $T_{\rm gw} \propto \Omega^{-8/3}_{\rm orb}$). As a result, $\Omega_{\rm asyn}$ slowly increases and the driving frequency gradually moves away from the mode resonance. This in turn reduces the torque and increases $T_{\rm s}$ until at some point (top edge of shaded regions in Fig. 12) the detuning becomes greater than the effective damping, $\Delta_a \gtrsim \gamma_{\rm eff}$. The torque then drops dramatically, $\Omega_{\rm s}$ stops increasing, and $\Omega_{\rm asyn}$ increases rapidly (entirely due to the GW-induced orbital decay). Eventually, $\Omega_{\rm asyn}$ gets so large that it hits the next mode resonance and the cycle begins again.

In the bottom panel of Fig. 11, we show $\dot{E}_{\rm diss}$ and $\dot{E}_{\rm tide}$ as a function of $P_{\rm orb}$. While the weakly non-linear model has a heating rate that is overall quite similar to the traveling-wave model (see also Section 5.4.1 below), it has brief but significant dips. Each dip corresponds to a transition from one resonant mode to the next

Downloaded from https://academic.oup.com/mnras/article/496/4/5482/5863236 by California Institute of Technology user on 22 October 2020

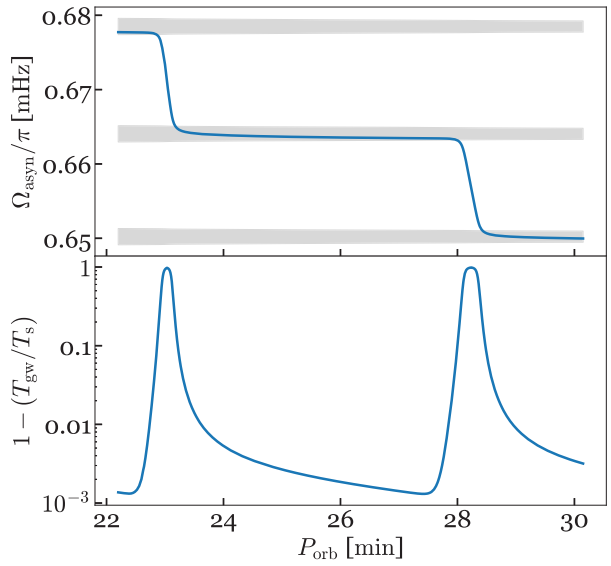

Figure 12. A zoomed-in view of the spin evolution in the weakly non-linear model when $P_{\rm orb} < P_{\rm c}^{\rm (nl)}$. The top panel shows the evolution of the asynchronicity, $\Omega_{\rm asyn}/\pi$. The shaded regions (from bottom to top) are centred on the eigenfrequencies of the $n_a = 48, 47, 46$ g-modes, with a width determined by the effective non-linear damping rate $\gamma_{\rm eff}$ (which increases slightly with decreasing $P_{\rm orb}$; see Section 5.3). The bottom panel shows $1 - (T_{\rm gw}/T_{\rm s})$, where $T_{\rm s}$ is the spin-up time-scale and $T_{\rm gw}$ is the GW-induced orbital decay time-scale.

(Fig. 12), during which the tidal heating is much less than the traveling-wave prediction given by equation (66) below.

In order to estimate the full width of each dip, first note that the driving frequency changes by $\Delta\omega = |\partial\omega_a/\partial n_a| \simeq \omega_a/n_a$ when evolving through the dip, where n_a (ω_a) is the radial order (eigenfrequency) of the mode prior to the transition. During the dip the orbit evolves much faster than the spin, and therefore $\Delta\omega \simeq m\Delta\Omega_{\rm orb} = 2\pi m|\Delta P_{\rm orb}|/P_{\rm orb}^2$. Since, as noted above, $\Omega_{\rm asyn}$ (and hence the driving frequency) evolves slowly for $P_{\rm orb} < P_{\rm c}$, we have $\omega_a \simeq \omega(P_{\rm orb} = P_{\rm c}) \simeq 2\pi m/P_{\rm c}$. Therefore, the width of the dip, i.e. the amount by which the orbital period changes during the dip, is

$$|\Delta P_{\rm orb}| \simeq \frac{P_{\rm orb}^2}{n_a P_{\rm c}}. \tag{62}$$

As we discuss in Section 6.1, the dips may have direct observational consequences, and may provide an explanation for the observed luminosity of the CO WD in J0651 (Brown et al. 2011; Hermes et al. 2012).

5.4.1 *Comparison with traveling-wave limit*

As with $\dot{E}_{\rm diss}$ in Section 5.3.5, it is useful to compare these weakly non-linear results to the traveling-wave results (even though the dynamical tide is a standing wave at $P_{\rm orb} \gtrsim 10$ min). According to the latter, $\dot{E}_{\rm diss}^{\rm (tw)} \propto \Omega_{\rm orb}^4\omega^6$ (equation 59). Thus, unlike our weakly non-linear results, $T_{\rm s}^{\rm (tw)} \propto \Omega_{\rm orb}^{-3}$ is steeper than $T_{\rm gw} \propto \Omega_{\rm orb}^{-8/3}$ and for $P_{\rm orb} < P_{\rm c}^{\rm (tw)}$ the asynchronicity is almost perfectly constant at a value $\Omega_{\rm asyn} \simeq 2\pi/P_{\rm c}^{\rm (tw)}$. Using our traveling-wave solution (Appendix C), we find

$$P_{\rm c}^{\rm (tw)} = 45\left(\frac{\hat{f}}{20}\right)^{3/16}\ {\rm min}. \tag{63}$$

More specifically, by plugging equations (35), (38)–(40), and (59) into the condition $\dot{\Omega}_{\rm s} \simeq \dot{\Omega}_{\rm orb}$, we find

$$\omega = 2\Omega_{\rm asyn} \propto \Omega_{\rm orb}^{-1/15}. \tag{64}$$

We thus see that even when the tidal torque is a smooth power law of the frequency, the asynchronicity can stay very nearly constant (it in fact decreases very slightly with increasing $\Omega_{\rm orb}$ to compensate for the excess tidal torque and maintain synchronization). BQAW13 argued that the torque needs to be a 'jagged' function of the driving frequency ω in order to maintain a resonance lock. While we agree that that is necessary in order to maintain an exact lock, i.e. $\dot{\Omega}_{\rm asyn} = 0$, equation (64) implies that even a torque that is a smooth, power-law function of ω has $\dot{\Omega}_{\rm asyn} \simeq 0$ and thus will, in effect, result in a lock.

5.4.2 *Tidal heating when synchronous*

When tidal synchronization does occur, the condition $\dot{\Omega}_{\rm s} \simeq \dot{\Omega}_{\rm orb}$ implies that the tidal energy transfer rate is dictated by the GW-induced decay rate and is essentially independent of the microphysics governing the dissipation process. In particular,

$$\dot{E}_{\rm tide} \simeq I_{\rm WD}\Omega_{\rm orb}\dot{\Omega}_{\rm orb,gw} \simeq \frac{3}{2}I_{\rm WD}\Omega_{\rm orb}^2\frac{\dot{E}_{\rm pp}}{E_{\rm orb}}, \tag{65}$$

where in the second equality we use the relation $\dot{\Omega}_{\rm orb,gw}/\Omega_{\rm orb} \simeq (3/2)\dot{E}_{\rm pp}/E_{\rm orb}$, with $\dot{E}_{\rm pp}$ the point-particle GW power and $E_{\rm orb} = -GMM/2D$ the orbital energy. The tidal heating rate is then given by

$$\dot{E}_{\rm diss} \simeq \frac{2\pi}{\Omega_{\rm orb}P_{\rm c}}\dot{E}_{\rm tide} \simeq \frac{2\pi}{P_{\rm c}}I_{\rm WD}\dot{\Omega}_{\rm orb,gw}, \tag{66}$$

with $I_{\rm WD}$ and $P_{\rm c}$ the only free parameters.

Note that even if we do not use the simple power-law fitting formula for the traveling-wave dissipation but take into account the scattering in the internal structure (see Fig. C1), the post-synchronization heating rate should still be a smooth function of frequency as demonstrated in fig. 14 of FL12. Varying the microphysics of the dissipation process (i.e. changing $\hat{f}$ or $\lambda_{\rm nl}$) only affects the post-synchronization heating rate through a change in the location of $P_{\rm c}$, which by equation (66) only changes the overall magnitude of the dissipation rate. And since $P_{\rm c}$ only depends weakly on $\hat{f}$ and $\lambda_{\rm nl}$ (see equations 61 and 63), the observed tidal heating should have a relatively small scattering for different CO WDs at a given orbital period $P_{\rm orb} < P_{\rm c}$. We discuss the observational implications of this in more detail in the next section.

6 OBSERVATIONAL SIGNATURES

6.1 In electromagnetic radiation

Tidal dissipation converts a fraction of the orbital energy into heat. In Appendix A2, we argue that the majority of the heat should be deposited at locations sufficiently close to the WD's surface where the thermal diffusion time-scale is much shorter than the orbital decay time-scale. As a result, we would expect the tidal heating to be instantly manifested at the surface and to play a significant role in determining the luminosity of WDs in compact binaries. This is especially true for systems with orbital periods $\lesssim$20 min, as we may expect the tidal heating to exceed the WD's intrinsic cooling (for a typical CO WD with an age of 1 Gyr, the luminosity due to its cooling is about $10^{-3}\,{\rm L}_\odot$; Salaris et al. 1997). Thus it would be particularly interesting to compare our prediction of the tidal heating rate to the

Downloaded from https://academic.oup.com/mnras/article/496/4/5482/5863236 by California Institute of Technology user on 22 October 2020

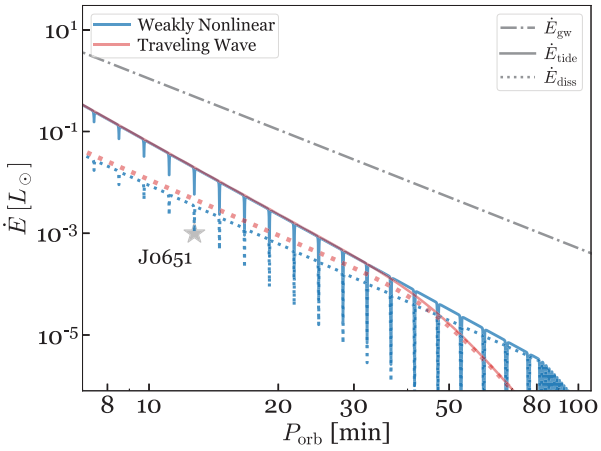

Figure 13. Similar to the bottom panel of Fig. 11 but for parameters corresponding to a J0651-like binary. We assume $M = 0.5\,{\rm M}_\odot$, $M' = 0.25\,{\rm M}_\odot$ and let the radius of the primary be $R = 9.9 \times 10^{-8}$ cm but keep the other parameters controlling the primary WD's internal structure the same as our main model. The star symbol is at the observed period and luminosity of J0651 (Hermes et al. 2012).

observed luminosity of the CO WD[11] in the 13-min system J0651 ($L = 1.0 \times 10^{-3}\,{\rm L}_\odot$ and $T_{\rm eff} = 8700\,{\rm K}$; Hermes et al. 2012).

We first consider the heating rates calculated under the traveling-wave model, which is appropriate for $P_{\rm orb} \lesssim 10$ min (see Section 3.5). As shown in FL12 and BQAW13, the traveling-wave calculation would predict a heating rate higher than the observed luminosity of the CO WD in J0651 by about a factor of 10. However, one of the key features of the traveling-wave model is that the heating rate should be a relatively smooth function of $P_{\rm orb}$ with little scatter. Because of the synchronization condition $\dot{\Omega}_{\rm s} \simeq \dot{\Omega}_{\rm orb}$, the heating rate is dictated by the GW radiation and should thus follow a smooth power law with respect to period. The only free parameters are the moment of inertia of the WD, $I_{\rm WD}$, and the asynchronicity period, $P_{\rm c}^{\rm (tw)}$ (see equation 66). The uncertainty in $I_{\rm WD}$ should be relatively small. Meanwhile, to increase $P_{\rm c}^{\rm (tw)}$ by a factor of 10 (in order to explain the luminosity of J0651), it would require an increase of $\hat{f}$, the characteristic traveling-wave dissipation rate, by a factor of 2.2×10^5 (see equation 63)!

On the other hand, our non-linear model offers a potential explanation of the observed luminosity of J0651 (though it may not be the only explanation). Recall from Fig. 11 that the non-linear model (blue traces) has a heating rate that is overall similar to the traveling-wave prediction when $10 < P_{\rm orb} < 20$ min, except that there are dips in the non-linear heating model when the asynchronicity transitions from one mode's resonance to the next.

In Fig. 13, we repeat the tidal heating calculation as we have done in Section 5.4. To generate the plot, we have adjusted the overall tidal amplitude ϵ according to J0651 (Hermes et al. 2012) so that $M = 0.5\,{\rm M}_\odot$ and $M' = 0.25\,{\rm M}_\odot$ for the primary and the secondary, respectively, and $R = 1.4 \times 10^{-2}\,{\rm R}_\odot = 9.9 \times 10^{-8}\,{\rm cm}$ (for the primary; the secondary is treated as a point mass). The other parameters determining the internal structure of the primary WD are left the same as our main WD model (see Section 3.1; this should be a good approximation as our model has a similar mass and effective temperature as the CO WD in J0651). We find a surprisingly good agreement between our non-linear model and the observation.[12]

While the exact match between our model and observation in Fig. 13 is a coincidence of our background model, we can none the less estimate the probability of observing such a system. In order to produce the low luminosity of J0651, it requires a system to be undergoing transition from one resonant mode to the other (see Fig. 12). In Fig. 13 it corresponds to the transition from parent mode $n_a = 67$ to 66. Thus the frequency difference between the two modes can be estimated as $|\partial\omega_a/\partial n_a| \simeq \omega_a/n_a$, corresponding to a width of the dip in terms of orbital period of $P_{\rm orb}^2/(n_a P_{\rm c}) \simeq 0.031$ min (equation 62). This gives the analytical approximation of the full width of the dip, and numerically we find a width of 0.021 min inside which the luminosity is within a factor of 2 of the local minimum. Meanwhile, the typical separation between two dips is about 1.7 min (the three dips closest to J0651 are, respectively, at orbital periods of 11.2, 12.8, and 14.5 min). Therefore, the probability of finding a system at a dip in the tidal heating is thus estimated to be $0.021/1.7 \simeq 1.2$ per cent.

We note that the parameter space can be further expanded if one takes into account the scattering in e.g. the tidal overlap of the parent mode Q_a, and/or the three-mode coupling coefficient κ_{abc} as they can make the dips deeper and hence a larger range of $P_{\rm orb}$ would be consistent with the observation. Note that the scattering in the internal structure affects the tidal heating only when $T_{\rm s} \gg T_{\rm gw}$, and therefore has little effect in the traveling-wave limit as argued above.

However, we cannot readily explain the luminosity of the recent observed 7-min system J1539 (Burdge et al. 2019). The model only allows for extra scattering towards the lower luminosity side of the traveling-wave model, which cannot be used to explain the higher than expected temperature of the CO WD in J1539. Moreover, the very low luminosity and temperature of the secondary WD in that system likely fall below our estimates (though we have not yet computed non-linear effects in He WD models). In general, it is difficult for tidal heating models to simultaneously explain the high luminosity of the primary and the low luminosity of the secondary in J1539, so it is likely that other effects such as ongoing mass transfer are occurring in that system.

Looking towards future, the nature of tidal dissipation can be better constrained when more compact WD binaries are observed by campaigns like the Extremely Low Mass (ELM; Brown et al. 2016) and Zwicky Transient Facility (ZTF; Graham et al. 2019) surveys. Whereas the traveling-wave model predicts the luminosities should follow a smooth power law with respect to the orbital period with small scatter, in the non-linear model we might expect occasional dips in the luminosity that are $\mathcal{O}(10)$ times fainter than the prediction of a smooth power law. The probability of seeing an underluminous system is estimated to be a few per cent, with the CO WD in J0651 potentially being one such example. A complication is that some WDs may be born at short orbital periods and still radiating their natal thermal energy, adding upward scatter to the observed temperatures. More discoveries at very short orbital periods ($P < 15$ min) where tidal heating dominates the luminosity will help test these ideas.

[11] We focus here only on the CO WD that is consistent with our background stellar model. We leave for future study the case of weakly non-linear dynamical tides of a He WD.

[12] It is also interesting to note that when the companion becomes less massive, the weakly non-linear model has a greater critical period than the traveling-wave model, $P_{\rm c}^{\rm (nl)} > P_{\rm c}^{\rm (tw)}$ when $y < 1$. This is because the weakly non-linear mode has a tidal dissipation rate that scales with the mass ratio y as $[2y/(1+y)]^{3/2}$, whereas in the traveling-wave model the scaling is $[2y/(1+y)]^2$; see equations (58) and (59).

Downloaded from https://academic.oup.com/mnras/article/496/4/5482/5863236 by California Institute of Technology user on 22 October 2020

6.2 In gravitational waves

The tidal interaction may lead to signatures in GWs that are potentially observable for proposed GW observatories like *LISA* (Kupfer et al. 2018; Korol et al. 2020) and *TianGO* (Kuns et al. 2019), whose detectability we estimate here. Our focus will be on systems that are sufficiently compact that their frequency chirping can be resolved by GW observatories over ∼5 yr. Moreover, we want the source to be individually resolvable instead of being part of the confusion foreground. This typically requires the system to start at a GW frequency $f_{\rm gw} > 3\,{\rm mHz}$, which corresponds to an orbital period $P_{\rm orb} < 11\,{\rm min}$. For those systems, the traveling-wave limit studied by FL12 begins to apply, as shown in Section 3.5. In fact, the best constraints on the tide will be derived from systems that are so compact that they are close to the onset of mass transfer.[13] In part, these systems are intrinsically louder in GW radiation compared to the less compact ones. Furthermore, as argued in equation (65), we have $\dot{E}_{\rm tide}/|\dot{E}_{\rm pp}| \propto \Omega_{\rm orb}^{4/3}$, and thus tidal effects play an increasingly important role relative to the point-particle GW radiation as the orbital frequency increases. More importantly, these systems will experience a significant amount of frequency evolution, which allows us to disentangle the point-particle effects and the tidal effects even if we do not know the binary's chirp mass a priori. To address this quantitatively, we will focus on binaries with $P_{\rm orb} \lesssim 5\,{\rm min}$ and adopt the Fisher information matrix to estimate the detectability of parameters, especially the WD moment of inertia, $I_{\rm WD}$. Our study compliments that by Piro (2019) who focused on systems at longer orbital periods near $P_{\rm orb} \simeq 10\,{\rm min}$. Such systems experience much less frequency evolution and thus only the leading-order frequency derivatives can be resolved.[14]

While in the case of inspiraling neutron star binaries, the leading-order effect on the gravitational waveform is due to the equilibrium tide (Flanagan & Hinderer 2008), it plays a comparatively minor role in the case of double WDs. To see why, first note that the energy of the equilibrium tide can be written as (BQAW13)

$$\frac{E_{\rm eq}}{E_0} = k_{\rm eq}\epsilon^2, \tag{67}$$

where the constant $k_{\rm eq} \equiv 2\sum_a W_a^2 Q_a^2 \simeq 0.07$, which is largely dominated by the f-mode contribution. The internal dissipation of the equilibrium tide induces a negligible tidal lag (Willems, Deloye & Kalogera 2010). Instead, the dominant contribution to the tidal lag is the GW-induced orbital decay (see e.g. Lai 1994). The associated energy transfer rate into the equilibrium tide (to raise the tidal bulge) is thus given by

$$\begin{aligned}\dot{E}_{\rm eq} &= \frac{2}{3}\frac{\dot{\Omega}_{\rm orb}}{\Omega_{\rm orb}} E_{\rm eq} \\ &= 2.0\times10^{-5}\,{\rm L}_\odot \left(\frac{k_{\rm eq}}{0.1}\right)\left(\frac{P_{\rm orb}}{10\,{\rm min}}\right)^{-20/3}.\end{aligned} \tag{68}$$

This is negligible compared to the energy transfer rate due to the dynamic tide (see Fig. 11), and we therefore ignore the effect of the equilibrium tide in the following discussion (see however the last paragraph of this section).

Since the systems we consider in this section are *in the traveling-wave regime*, we expect the WD's spin to be well synchronized with the orbit and thus $\dot{\Omega}_{\rm orb} \simeq \dot{\Omega}_{\rm s}$. We can solve for the excess frequency evolution due to the dynamical tide $\dot{\Omega}_{\rm tide} \equiv \dot{\Omega}_{\rm orb} - \dot{\Omega}_{\rm orb,gw}$ by using the relations given in Section 3.4 and the fact that the post-synchronization dynamical tide is essentially controlled by a single parameter, $I_{\rm WD}$ (Section 5.4.1), and is therefore insensitive to the details of the tidal interaction (namely, the value of $\hat{f}$). We find

$$\dot{\Omega}_{\rm tide} = \dot{\Omega}_{\rm orb} - \dot{\Omega}_{\rm orb,gw} = \left(\frac{3I_{\rm WD}/I_{\rm orb}}{1-3I_{\rm WD}/I_{\rm orb}}\right)\dot{\Omega}_{\rm orb,gw}, \tag{69}$$

where $I_{\rm orb}$ is the orbital moment of inertia, and for future convenience we express it in terms of $\mathcal{M}_{\rm c}$ and $\Omega_{\rm orb}$ as

$$I_{\rm orb} = \mu D^2 = \frac{G^{2/3}\mathcal{M}_{\rm c}^{5/3}}{\Omega_{\rm orb}^{4/3}}. \tag{70}$$

The Fisher matrix analysis is most conveniently done in the frequency domain. This requires finding the phase $\Psi(f_{\rm gw})$ of the GW waveform in the frequency domain, which is related to the time-domain GW phase $\phi(t)$ as (Cutler & Flanagan 1994)

$$\Psi(f_{\rm gw}) = 2\pi f_{\rm gw} t(f_{\rm gw}) - \phi\left[t(f_{\rm gw})\right] - \frac{\pi}{4}. \tag{71}$$

Separating the GW frequency evolution into the point-particle contribution $\dot{f}_{\rm pp} = \dot{\Omega}_{\rm orb,gw}/\pi$ and the tide-induced contribution $\dot{f}_{\rm tide} = \dot{\Omega}_{\rm tide}/\pi$, we have

$$\begin{aligned}t(f_{\rm gw}) &= \int^{f_{\rm gw}} \frac{{\rm d}f}{\dot{f}} = \int^{f_{\rm gw}} \frac{{\rm d}f}{\dot{f}_{\rm pp}+\dot{f}_{\rm tide}} \\ &= t_{\rm pp}(f_{\rm gw}) - \int^{f_{\rm gw}} \frac{3I_{\rm WD}}{I_{\rm orb}}\frac{{\rm d}f}{\dot{f}_{\rm pp}},\end{aligned} \tag{72}$$

where $t_{\rm pp}(f_{\rm gw}) = \int {\rm d}f_{\rm gw}/\dot{f}_{\rm pp}$ is the time as a function of GW frequency without tidal effects and we use equation (70) to derive the last equality. The lower limit of the integration (not shown) is set to be the initial frequency of the waveform. Similarly, the time-domain phase can be evaluated as

$$\begin{aligned}\phi\left[t(f_{\rm gw})\right] &= 2\pi\int^{f_{\rm gw}} \frac{f}{\dot{f}}{\rm d}f \\ &= \phi_{\rm pp}\left[t(f_{\rm gw})\right] - 2\pi\int^{f_{\rm gw}} \frac{3I_{\rm WD}}{I_{\rm orb}}\frac{f}{\dot{f}_{\rm pp}}{\rm d}f,\end{aligned} \tag{73}$$

where $\phi_{\rm pp}$ is the point-particle phase. Consequently, we have

$$\begin{aligned}\Psi(f_{\rm gw}) = \Psi_{\rm pp}(f_{\rm gw}) - 2\pi\Bigg(&f_{\rm gw}\int^{f_{\rm gw}} \frac{3I_{\rm WD}}{I_{\rm orb}}\frac{{\rm d}f}{\dot{f}_{\rm pp}} \\ &- \int^{f_{\rm gw}} \frac{3I_{\rm WD}}{I_{\rm orb}}\frac{f}{\dot{f}_{\rm pp}}{\rm d}f\Bigg).\end{aligned} \tag{74}$$

Even at the onset of mass transfer ($f_{\rm gw} \simeq 30\,{\rm mHz}$ for a typical 0.6–0.6 WD binary), the orbital velocity $(v_{\rm orb}/c)^2 \lesssim 10^{-4}$. Thus the leading-order quadruple formula is sufficient to describe the point-particle phase $\Psi_{\rm pp}$, which is given by

$$\Psi_{\rm pp}(f_{\rm gw}) = 2\pi f_{\rm gw} t_{\rm c} - \phi_{\rm c} - \frac{\pi}{4} - \frac{3}{4}\left(\frac{8\pi G}{c^3}\mathcal{M}_{\rm c} f_{\rm gw}\right)^{5/3}, \tag{75}$$

where $t_{\rm c}$ and $\phi_{\rm c}$ are constants of integration. Since the orbital moment of inertia $I_{\rm orb}$ can be viewed as function of $f_{\rm gw}$, with the

[13] For a typical 0.6–0.6 WD binary, the onset of the Roche lobe overflow corresponds to a GW frequency of 30 mHz and $P_{\rm orb} = 1.1\,{\rm min}$.

[14] Assuming a 5-yr observation, the frequency resolution is 6.3 nHz. Over this period, a system initially at $P_{\rm orb} \simeq 10\,{\rm min}$ ($f_{\rm gw} \simeq 3\,{\rm mHz}$) evolves only ∼25 nHz. In comparison, the systems we consider in this section will evolve by an amount ranging from ∼1 μHz, if the initial GW frequency is $f_{\rm gw} = 10\,{\rm mHz}$, to ∼100 μHz, if the initial frequency is $f_{\rm gw} = 30\,{\rm mHz}$.

Downloaded from https://academic.oup.com/mnras/article/496/4/5482/5863236 by California Institute of Technology user on 22 October 2020

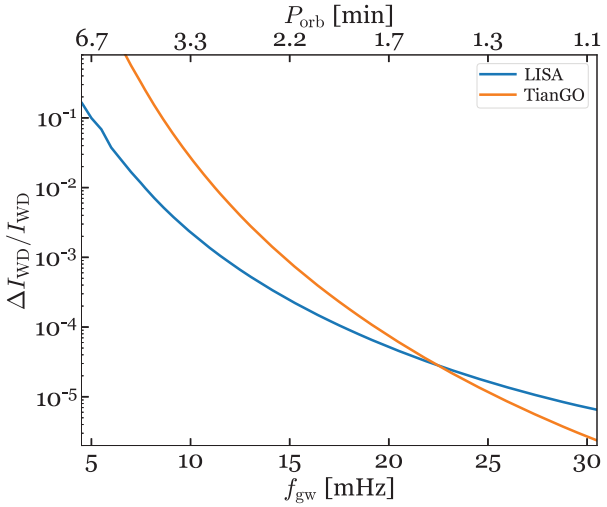

Figure 14. Fractional uncertainty on the WD's moment of inertia as a function of the binary's GW frequency over an observational period of 5 yr. We assume the binary is at a distance of 10 kpc and we averaged over its sky location. Note that we focus here on binaries with very short orbital periods, and hence assume that the system is in the traveling-wave regime and the spin is synchronized with the orbit ($\dot{\Omega}_{\rm s} = \dot{\Omega}_{\rm orb}$).

chirp mass $\mathcal{M}_{\rm c}$ a parameter (see equation 70), we can construct the frequency-domain strain waveform $h(f_{\rm gw})$ with five parameters,[15] $\{r, \mathcal{M}_{\rm c}, t_{\rm c}, \phi_{\rm c}, I_{\rm WD}\}$, where r is the distance to the source. Note that so far we only included the tidal effect from one of the WDs; in reality, both WDs contribute to the phase shift and the quantity we measure will be the sum of their moments of inertia.[16]

In Fig. 14, we show the fractional measurement uncertainty of the WD's moment of inertia as a function of the binary's GW frequency. The x-axis gives the binary's *initial* GW frequency, and we show results assuming a 5-yr observation. We fix the source distance at 10 kpc and adopt the Fisher matrix technique to calculate the parameter estimation uncertainty using both the sky-averaged *LISA* (blue) and *TianGO* (orange) sensitivities. We see that for a WD at $f_{\rm gw} = 10\,{\rm mHz}$, *LISA* can already constrain the moment of inertia to better than 0.1 per cent. For a system close to the onset of Roche lobe overflow, the statistical uncertainty in $I_{\rm WD}$ with *TianGO*'s sensitivity can be as small as 10^{-6}. In reality, this precision may not be reached because the modelling assumptions of this section (such as the assumption of spin–orbit synchronization) introduce systematic errors. None the less, it is clear that future space-based GW observatories will be able to detect the tide's contribution to the orbital decay, which will constrain the WD moments of inertia and theories of tidal dissipation.

While here we have treated the moment of inertia $I_{\rm WD}$ as a free parameter, in the near future we may have a sufficiently reliable model of WDs (especially after verifying the tidal effect after the first few detections by *LISA* and/or *TianGO* with high statistical accuracy). If, for example, we can treat the moment of inertia as a function of mass, $I_{\rm WD} = I_{\rm WD}(M)$, instead of as a free parameter, then the tidal effect will allow us to measure the component masses of the binary instead of just chirp mass (see equation 74). This will help improve our understanding of Type Ia supernovae and their progenitors as it allows us to measure a binary's total mass and determine whether it is super- or sub-Chandrasekhar. This possibility was also demonstrated by Kuns et al. (2019).

Lastly, while here we focus on the effects of dynamical tides on the secular evolution of the binary, McNeill, Mardling & Müller (2020) recently proposed an alternative method of constraining the WD structure using the equilibrium tide. Specifically, the equilibrium tide introduces a non-dissipative radial force $-\partial H/\partial D \sim {\rm Re}\left[q_a^* U\right]$ (see equation 31). This force causes a *non-secular* oscillation of the orbital eccentricity, which generates GWs at both $\Omega_{\rm orb}$ and $3\Omega_{\rm orb}$ in addition to the main $2\Omega_{\rm orb}$ harmonic. Since the effect proposed by McNeill et al. (2020) operates on a time-scale of $P_{\rm orb}$ whereas the dynamical tide is manifested over a much longer time-scale $\sim T_{\rm gw}$, we expect the two effects to be complementary to each other. The eccentricity excited by the equilibrium tide might further enhance the dynamical tide's dissipation rate, as the spin is not synchronized with the first and third orbital harmonics, and it could thus further excite waves inside the WDs. We plan to study this interaction in the future.

7 SUMMARY AND DISCUSSION

In this paper, we studied the effects of non-linear dynamical tides in compact WD binaries that inspiral due to GW radiation. Our focus was on the weakly non-linear regime that we showed covers the orbital period range $10 \lesssim P_{\rm orb}/{\rm min} \lesssim 150$ (see Fig. 5). In this range, parent modes resonantly driven by the linear tide are so energetic that they excite secondary waves through the three-mode parametric instability. At longer periods linear theory applies, and at shorter periods the parents are driven to such large amplitudes that they become strongly non-linear and break near the WD's surface. Such parents are therefore traveling waves rather than standing waves.

To study the weakly non-linear regime, we carried out a suite of numerical integrations of coupled mode networks over a wide range of orbital periods. The duration of each integration was a few non-linear growth times $T_{\rm nl} \ll T_{\rm gw}$, where $T_{\rm gw}$ is the GW decay time-scale. On this time-scale, the system settled into a quasi-steady state in which the total mode energy and energy dissipation rate approached constant values. We considered mode networks with 32 and 92 modes, both consisting of five mode generations, and found that they converged on similar values for the total energy dissipation rate. The computed dissipation rates are orders of magnitude larger than that predicted by linear theory.

Based on the mode network integrations, we constructed phenomenological models that provided a robust estimate of the non-linear dissipation rate as a function of the system parameters (Section 5.2). In the models, the total energy dissipation rate is given by the product of an effective damping rate $\gamma_{\rm eff}$ and an effective energy $E_{\rm eff}$. The effective damping is characterized by the three-mode parametric growth rate $\Gamma_{\rm nl}$ (equation 46) that is itself a function of mode energy. The effective energy has a Lorentzian profile like the linear tide energy but with $\gamma_{\rm eff}$ replacing the linear damping rate γ_a (see equations 25 and 56). They are approximately equal when the frequency detuning is large ($\Delta_a > \gamma_{\rm eff} \gg \gamma_a$), while $E_{\rm eff}$ is always much smaller than the total mode energy in the non-linear network [their ratio is $\mathcal{O}(\gamma_a/\Gamma_{\rm nl}) \ll 1$].

[15]Here we focus on the detectability of intrinsic parameters, so we have dropped the inclination, polarization, and sky location of the source, and use the sky-averaged sensitivity curves of *LISA* and *TianGO* (see fig. 1 of Kuns et al. 2019).

[16]Note that the WD's moment of inertia enters the phase linearly. Therefore the parameter estimation uncertainty on the moment of inertia, $\Delta I_{\rm WD}$, is independent of the magnitude of $I_{\rm WD}$, whereas the fractional error $\Delta I_{\rm WD}/I_{\rm WD}$ decreases as $I_{\rm WD}$ increases.

Downloaded from https://academic.oup.com/mnras/article/496/4/5482/5863236 by California Institute of Technology user on 22 October 2020

We used the dissipation models to analyse the tidal synchronization and heating of a CO WD as a function of orbital separation. Although the trajectories in the weakly non-linear, standing wave regime are similar to what previous studies found by (incorrectly) assuming a traveling wave at $P_{\rm orb} > 10$ min, there are some important differences. The most significant difference is that in the weakly non-linear analysis, there are brief dips in the tidal heating rate that are 10–100 times below the traveling-wave estimates (see Figs 11 and 13). This is because in our weakly non-linear model, tidal synchronization can only be approximately achieved for a finite duration near a resonance peak (Fig. 12). Once the tidal torque at resonance becomes insufficient to synchronize the spin with the orbit, the asynchronicity $\Omega_{\rm asyn} = (\Omega_{\rm orb} - \Omega_{\rm s})$ increases, and the mode moves out of resonance. As a result, the total tidal torque and heating rate drop significantly until the next mode becomes resonant.

These dips offer a potential explanation for the observed luminosity of the CO WD in J0651 (see Fig. 13), which is about 10 times fainter than predicted by the traveling-wave model. On the other hand, the probability of finding a WD in such a state is only a few per cent based on the width and spacing of the dips. The recently observed 7-min system J1539 has an especially high luminosity that cannot be explained by our model, although it is likely in the traveling-wave regime and other non-tidal effects, such as ongoing or previous mass transfer, are likely at play in this system.

More generally, we predict that most WD binaries with orbital periods between about 10 and 20 min will have a luminosity L consistent with the traveling-wave model and follow a power-law scaling with respect to the orbital period, $L \simeq \dot{E}_{\rm diss} \propto P_{\rm orb}^{-11/3}$ (equation 66). However, we expect $\mathcal{O}$(1 per cent) will be outliers that are 10 times dimmer. Future surveys should be able to test this idea.

Lastly, we considered the impact of dynamical tides on the GW signal. Since the loudest sources will have $P_{\rm orb} < 10$ min, in this part of the analysis we adopted the traveling-wave model and assumed that the WD spin would be synchronized with the orbit. We showed that under these assumptions the only free parameter impacting the GW signal is the moment of inertia of the WD (or the sum of the moments of inertia if the tides in both WDs are taken into account). We found that the moment of inertia should be constrained to better than 1 per cent with future space-based GW observatories like *LISA* or *TianGO*.

Our mode coupling formalism and network integrations assumed that all the excited modes are standing waves. Although we showed that the parent mode does not break for $P_{\rm orb} \gtrsim 10$ min and is therefore a standing wave, it is less clear whether the same is true of the secondary waves that the parent excites. Since the shear increases with increasing wavenumber, the secondary waves break at a smaller energy than the parent. On the other hand, they are parametrically unstable to three-mode coupling at a smaller energy than the parent. As our network integrations show, three-mode coupling can suppress mode amplitudes and prevent them from reaching wave-breaking energies (e.g. we find that the parent's energy at resonance peaks is suppressed by orders of magnitude compared to the linear value as a result of three mode coupling; see Fig. 9). Addressing this issue in detail requires a formalism that allows for a mix of coupled standing waves and traveling waves. Such an analysis might be especially important for very hot WDs since the shear and linear damping rates increase with increasing temperature and thus the tide is more likely to excite traveling waves.

Throughout our analysis, we assumed that the WD can maintain solid-body rotation throughout its evolution, and we accounted for the spin's effect only on the Doppler shift of the tidal driving frequency. In particular, we neglected the Coriolis and centrifugal effects of rotation on the WD's oscillation modes.

One of the rotational effects is the shift of a mode's eigenfrequency. To account for this effect, the condition for resonant locking should be generalized as (Witte & Savonije 1999; BQAW13)

$$0 \simeq m\left(\dot{\Omega}_{\rm orb} - \dot{\Omega}_{\rm s}\right) - \dot{\omega}_a = m\left[\dot{\Omega}_{\rm orb} - \left(1 + \frac{1}{m}\frac{\partial \omega_a}{\partial \Omega_{\rm s}}\right)\dot{\Omega}_{\rm s}\right]. \quad (76)$$

Under the traditional approximation of rotation, we have $\partial\omega_a/\partial\Omega_{\rm s} \simeq -m/6$ in the slow-rotation limit (Unno et al. 1989; BQAW13). Such a constant does not affect the qualitative synchronization trajectory we considered in Section 5. Higher order corrections to the mode frequency and the rotational modifications to the tidal overlap (Ivanov et al. 2013) and to the three-mode coupling (Schenk et al. 2002) may also be important, but are ignored in the current study for simplicity. Nevertheless, Fuller & Lai (2014) showed that in the traveling-wave limit, rotation does not significantly alter the spin-up and heating trajectories of inspiraling WDs.

Another critical simplification we made is that we fixed the background model and ignored any potential adjustments to the structure due to tidal heating. While this treatment is also adopted by previous studies (e.g. FL12; BQAW13), its validity remains to be examined more carefully, especially when the tidal heating rate is significantly greater than the WD's intrinsic cooling luminosity. This effect may further change the synchronization trajectory, equation (76), by introducing terms such as $(\partial\omega_a/\partial T_{\rm eff})\dot{T}_{\rm eff}$. We plan to study this effect in future work.

ACKNOWLEDGEMENTS

The authors thank Yanbei Chen, Dong Lai, and Pavel Ivanov for valuable discussions and comments. This work made use of the High Performance Computing resources at MIT Kavli Institute. HY is supported by the Sherman Fairchild Foundation. NNW acknowledges support from the NSF through grant AST-1909718.

DATA AVAILABILITY

The MESA inlists to generate the background WD model and the data underlying this paper will be shared on reasonable request to the corresponding author.

REFERENCES

Amaro-Seoane P. et al., 2017, preprint (arXiv:1702.00786)
Barker A. J., 2011, MNRAS, 414, 1365
Barker A. J., Ogilvie G. I., 2011, MNRAS, 417, 745
Brink J., Teukolsky S. A., Wasserman I., 2005, Phys. Rev. D, 71, 064029
Brown W. R., Kilic M., Hermes J. J., Allende Prieto C., Kenyon S. J., Winget D. E., 2011, ApJ, 737, L23
Brown W. R., Gianninas A., Kilic M., Kenyon S. J., Allende Prieto C., 2016, ApJ, 818, 155
Burdge K. B. et al., 2019, Nature, 571, 528
Burkart J., Quataert E., Arras P., Weinberg N. N., 2013, MNRAS, 433, 332 (BQAW13)
Clayton G. C., 2012, J. Am. Assoc. Var. Star Obser., 40, 539
Cutler C., Flanagan E. E., 1994, Phys. Rev. D, 49, 2658
Dan M., Rosswog S., Brüggen M., Podsiadlowski P., 2014, MNRAS, 438, 14
Essick R., Weinberg N. N., 2016, ApJ, 816, 18 (EW16)
Fenn D., Plewa T., Gawryszczak A., 2016, MNRAS, 462, 2486
Ferrario L., de Martino D., Gänsicke B. T., 2015, Space Sci. Rev., 191, 111
Flanagan É. É., Hinderer T., 2008, Phys. Rev. D, 77, 021502
Fuller J., Lai D., 2011, MNRAS, 412, 1331

Downloaded from https://academic.oup.com/mnras/article/496/4/5482/5863236 by California Institute of Technology user on 22 October 2020

Fuller J., Lai D., 2012a, MNRAS, 421, 426 (FL12)
Fuller J., Lai D., 2012b, ApJ, 756, L17
Fuller J., Lai D., 2013, MNRAS, 430, 274
Fuller J., Lai D., 2014, MNRAS, 444, 3488
Goodman J., Dickson E. S., 1998, ApJ, 507, 938
Graham M. J. et al., 2019, PASP, 131, 078001
Hermes J. J. et al., 2012, ApJ, 757, L21
Iben I., Jr, Tutukov A. V., 1984, ApJS, 54, 335
Iben I., Jr, Tutukov A. V., Fedorova A. V., 1998, ApJ, 503, 344
Ivanov P. B., Papaloizou J. C. B., Chernov S. V., 2013, MNRAS, 432, 2339
Korol V. et al., 2020, A&A, 638, A153
Kumar P., Goodman J., 1996, ApJ, 466, 946
Kuns K. A., Yu H., Chen Y., Adhikari R. X., 2019, preprint (arXiv:1908.06004)
Kupfer T. et al., 2018, MNRAS, 480, 302
Lai D., 1994, MNRAS, 270, 611
Lam S. K., Pitrou A., Seibert S., 2015, in Proceedings of the Second Workshop on the LLVM Compiler Infrastructure in HPC (LLVM 2015). Association for Computing Machinery (ACM), New York (https://doi.org/10.1145/2833157.2833162)
Luo J. et al., 2016, Classical Quantum Gravity, 33, 035010
McNeill L. O., Mardling R. A., Müller B., 2020, MNRAS, 491, 3000
Nelemans G., Portegies Zwart S. F., Verbunt F., Yungelson L. R., 2001, A&A, 368, 939
Ogilvie G. I., Lin D. N. C., 2007, ApJ, 661, 1180
Paxton B., Bildsten L., Dotter A., Herwig F., Lesaffre P., Timmes F., 2011, ApJS, 192, 3
Paxton B. et al., 2013, ApJS, 208, 4
Paxton B. et al., 2015, ApJS, 220, 15
Paxton B. et al., 2018, ApJS, 234, 34
Piro A. L., 2019, ApJ, 885, L2
Polin A., Nugent P., Kasen D., 2019a, preprint (arXiv:1910.12434)
Polin A., Nugent P., Kasen D., 2019b, ApJ, 873, 84
Press W. H., Teukolsky S. A., 1977, ApJ, 213, 183
Raskin C., Scannapieco E., Fryer C., Rockefeller G., Timmes F. X., 2012, ApJ, 746, 62
Salaris M., Domínguez I., García-Berro E., Hernanz M., Isern J., Mochkovitch R., 1997, ApJ, 486, 413
Schenk A. K., Arras P., Flanagan É. É., Teukolsky S. A., Wasserman I., 2002, Phys. Rev. D, 65, 024001
Shen K. J., Kasen D., Miles B. J., Townsley D. M., 2018, ApJ, 854, 52
Shiode J. H., Quataert E., Arras P., 2012, MNRAS, 423, 3397
Timmes F. X., Townsend R. H. D., Bauer E. B., Thoul A., Fields C. E., Wolf W. M., 2018, ApJ, 867, L30
Toonen S., Nelemans G., Portegies Zwart S., 2012, A&A, 546, A70
Townsend R. H. D., Teitler S. A., 2013, MNRAS, 435, 3406
Townsend R. H. D., Goldstein J., Zweibel E. G., 2018, MNRAS, 475, 879
Unno W., Osaki Y., Ando H., Saio H., Shibahashi H., 1989, Nonradial Oscillations of Stars, 2nd edn. Univ. Tokyo Press, Tokyo
Venumadhav T., Zimmerman A., Hirata C. M., 2014, ApJ, 781, 23
Webbink R. F., 1984, ApJ, 277, 355
Weinberg N. N., 2016, ApJ, 819, 109
Weinberg N. N., Arras P., Quataert E., Burkart J., 2012, ApJ, 751, 136 (WAQB12)
Willems B., Deloye C. J., Kalogera V., 2010, ApJ, 713, 239
Witte M. G., Savonije G. J., 1999, A&A, 350, 129
Wu Y., Goldreich P., 2001, ApJ, 546, 469

APPENDIX A: ASYMPTOTIC RELATIONS

In this appendix, we present various asymptotic relations used in our calculations. For future convenience, we expand the Lagrangian displacement vector field $\boldsymbol{\xi}_a$ as

$$\boldsymbol{\xi}_a(\boldsymbol{r}) = \left[\xi_a^r(r)\boldsymbol{e}_r + \xi_a^h(r) r\nabla\right] Y_{l_a m_a}(\theta,\phi), \tag{A1}$$

where $\boldsymbol{e}_r$ is the unit vector along the radial direction. The radial and horizontal motions can thus be characterized by $\xi_a^r(r)$ and $\xi_a^h(r)$, respectively.

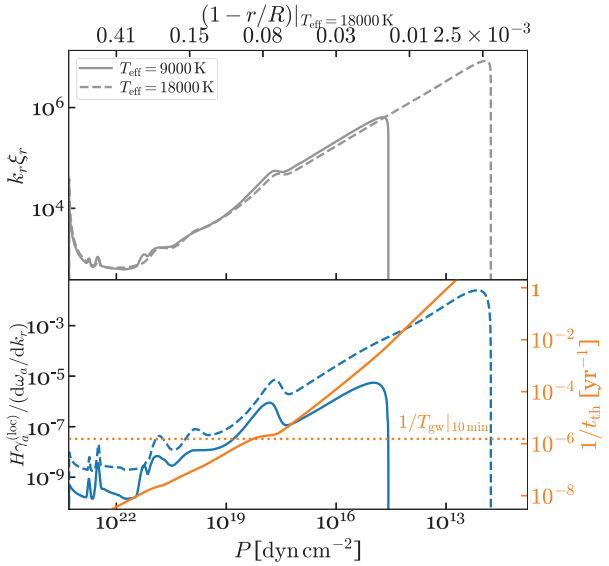

Figure A1. Top panel: profile of the shear envelope $k_r A$ for a normalized mode with $q_a = 1$. Bottom panel: local damping rate weighted by the time the wave spends per scale height (blue line) and time-scales for thermal diffusion (solid orange line) and GW-driven orbital decay (dotted orange line). We show results for both our standard CO WD model with $T_{\rm eff} = 9000$ K (solid lines) and a hotter CO WD model with $T_{\rm eff} = 18\,000$ K (dashed lines). We set $\omega_a = 0.01\omega_0$ here; for the range of interest, varying ω_a modifies the overall scale but has almost no effect on the shape of the profile.

A1 Shear profile

For a high-order g-mode normalized according to equation (10), the radial displacement ξ_a^r can be approximated by the Wentzel–Kramers–Brillouin (WKB) relation (Unno et al. 1989)

$$\xi_a^r \simeq A\sin\phi, \tag{A2}$$

where the phase $\phi = \int k_r \mathrm{d}r + \pi/4$ and the amplitude

$$A^2 = \left(\frac{E_0}{\int \mathcal{N}\,\mathrm{d}\ln r}\right)\frac{1}{\rho r^3 \mathcal{N}}. \tag{A3}$$

Consequently, we can approximate the envelope of the shear as a function of radius as $|k_r\xi_a^r| \sim k_r A$ with the wavenumber k_r given by equation (3).

In Fig. A1, we show the shear profile. When evaluating k_r, we assume a reference frequency $\omega_a = 0.01\omega_0$. Notice that the amplitude A is determined purely by background quantities while the wavenumber $k_r \propto 1/\omega_a$ when $\omega_a^2 \ll \mathcal{N}^2, S_l^2$. Therefore, different g-modes (as well as the traveling-wave solution) will have essentially the same shape as the shear envelope, which peaks at a radius $r = 0.994R$ and a pressure $P = 5.4\times10^{14}$ dyn cm^{-2} for the $T_{\rm eff} = 9000$ K model we consider in the main text (corresponding to the solid traces in Fig. A1; note that this is different from solar models where the wave breaks near the centre; see e.g. Ogilvie & Lin 2007; Barker & Ogilvie 2011; WAQB12; EW16). The maximum shear over the star (which we used to derive the threshold energy of local wave breaking in Fig. 5) can then be expressed as

$$\max_r |q_a k_r \xi_a^r| = \max_r |q_a k_r A| \simeq 6.4\times10^5 q_a \left(\frac{0.01\omega_0}{\omega_a}\right), \tag{A4}$$

where the numerical value is for the $T_{\rm eff} = 9000$ K model.

Downloaded from https://academic.oup.com/mnras/article/496/4/5482/5863236 by California Institute of Technology user on 22 October 2020

While in the main text we focus on a single WD model with $T_{\rm eff}$=9000 K, in Fig. A1 we also consider a model with $T_{\rm eff}$=18 000 K. As the WD becomes hotter, the radiative zone extends closer to the surface. Thus, a gravity wave of a given frequency propagates out to smaller pressures and its peak shear can be greater. Consequently, tidal heating might further accelerate the transition between the weakly-non-linear tidal interaction to the traveling-wave limit as the binary's separation decreases. Assessing this possibility requires a study that couples tidal effects to the adjustment of the WD's internal structure.

A2 Linear dissipation

We now describe our calculation of the dissipation rates, which closely follows the work of BQAW13.

There are two types of mode damping that are potentially relevant in the WD. The first is due to electron conduction and radiative diffusion, which can be estimated as

$$\gamma_a^{(\rm diff)} = \frac{\omega_a^2}{E_0}\int \chi k_r^2 \left[\left(\xi_a^r\right)^2 + l(l+1)\left(\xi_a^h\right)^2\right]\rho r^2 {\rm d}r, \tag{A5}$$

where the thermal diffusivity

$$\chi = \frac{16\sigma T^3}{3\kappa\rho^2 C_P}. \tag{A6}$$

Here κ and C_P are the opacity and the specific heat at constant total pressure. In addition to thermal diffusion, a g-mode can also be damped by convective turbulence, whose dissipation rate we estimate as

$$\gamma_a^{(\rm turb)} = \frac{\omega_a^2}{E_0}\int \nu_{\rm turb}\left[0.23\left(\frac{{\rm d}\xi_a^r}{{\rm d}r}\right)^2 + 0.084 l(l+1)\left(\frac{{\rm d}\xi_a^h}{{\rm d}r}\right)^2\right]\rho r^2 {\rm d}r, \tag{A7}$$

where $\nu_{\rm turb}$ is the effective turbulent viscosity (Shiode, Quataert & Arras 2012),

$$\nu_{\rm turb} = L_{\rm c} v_{\rm c} \min\left[10\left(\frac{2\pi L_{\rm c}}{\omega_a v_{\rm c}}\right)^2, \left(\frac{2\pi L_{\rm c}}{\omega_a v_{\rm c}}\right), 2.4\right]. \tag{A8}$$

Here $L_{\rm c}$ and $v_{\rm c}$ are the convective luminosity and velocity according to mixing length theory (which are given by our MESA model).

In Fig. 2, we present the dissipation rates as a function of the mode radial order (bottom axis) and frequency (top axis). The dots are exact values calculated under the prescription described in this section, and the solid lines are the power-law fits given in Section 3.1. The blue and green lines are the dissipation due to thermal diffusion and turbulent damping, and the orange line is the inverse of a mode's group travel time (see equation 42). We see that for modes with $n_a \gtrsim 20$, the dissipation is dominated by thermal diffusion. Those are the modes most relevant for the tidal synchronization calculation. For modes with lower radial orders, the turbulent damping becomes significant. We do not include the contribution of $\gamma_a^{(\rm turb)}$ in our mode network calculations since modes with $n_a \lesssim 20$ are not excited once the tidal synchronization is taken into account (see Section 5.4).

The quantity presented in equation (A5) is the *global* damping rate. To better understand the tidal heating process, it is also instructive to study the *local* heating rate, $\gamma_a^{(\rm loc)}=\chi k_r^2/2$. Specifically, the global damping rate can be viewed as the integral of the local rate weighted by the time the wave packet spends at each radius (Goodman & Dickson 1998),

$$\gamma_a^{(\rm diff)} \simeq \frac{2}{T_a}\int \gamma_a^{(\rm loc)}\frac{{\rm d}r}{{\rm d}\omega_a/{\rm d}k_r} = \frac{2}{T_a}\int \gamma_a^{(\rm loc)}\frac{H}{{\rm d}\omega_a/{\rm d}k_r}{\rm d}\ln P, \tag{A9}$$

where $T_a = 2\int {\rm d}r({\rm d}\omega_a/{\rm d}k_r)^{-1}$ is the wave's group travel time and $H \equiv P/g\rho$ is the pressure scale height.[17] In the second line, we reversed the limits of integration so that it corresponds to increasing $\ln P$. In the lower panel of Fig. A1, we show the integrand of equation (A9). Note that by presenting it in this form (local damping rate weighted by the time the wave packet spends per pressure scale height), we expect an equal contribution to the total damping per d$\ln P$. The figure assumes a reference frequency $\omega_a = 0.01\omega_0$ and the solid and dashed blue lines represent the $T_{\rm eff} = 9000$ K and $T_{\rm eff} = 18\,000$ K models, respectively. Note that similar to the shear profile, the reference frequency ω_a only affects the overall magnitude of the damping but does not change its shape. The solid orange line shows the inverse of the local thermal diffusion time-scale,

$$t_{\rm th} = \frac{PC_PT}{gF}, \tag{A10}$$

for the $T_{\rm eff} = 9000$ K model, where F is the radiation flux (the $T_{\rm eff} = 18\,000$ K model has a similar $t_{\rm th}^{-1}$ profile). As a reference, the dotted orange line is the inverse of the GW decay time-scale for a binary at $P_{\rm orb} = 10$ min (see equation 48).

As Fig. A1 shows the peak of the weighted local damping rate happens near the WD surface at a location close to the peak of the shear. The typical thermal time-scale at the peak is less than 1000 yr, and all the heat deposited at $P \lesssim 10^{18}$ dyne cm^{-2} has $t_{\rm th} < T_{\rm gw}$. Therefore, a significant portion of the tidal heating can diffuse out through the surface layers and hence affect the observed luminosity of WDs in compact binaries.

A3 Tidal overlap

For the high-order g-modes that we consider, a brute-force calculation of the tidal overlap Q_a according to equation (23) is subject to considerable numerical error as the modes are highly oscillatory. A more numerically accurate approach is to evaluate it in terms of the equilibrium tide solution (see also equations C4 and C5; BQAW13),

$$\boldsymbol{f}_1\left[\boldsymbol{\xi}_{\rm eq}(\boldsymbol{r})\right] \equiv \rho W_{lm}\frac{GM'}{D^{l+1}}\nabla\left(r^l Y_{lm}\right). \tag{A11}$$

We further note that the set of linear eigenmodes $\{\boldsymbol{\xi}_a\}$ forms a complete, orthonormal basis. This allows us to expand the equilibrium tide as

$$\boldsymbol{\xi}_{\rm eq}(\boldsymbol{r}) = \sum x_a \boldsymbol{\xi}_a(\boldsymbol{r}). \tag{A12}$$

Applying first the $\boldsymbol{f}_1$ operation on both side of equation (A12) and then contracting with $\boldsymbol{\xi}_a$ using the orthogonality equation (10), we can express the expansion coefficient x_a in terms of the tidal overlap integral,

$$x_a = \epsilon W_{lm} Q_{alm}. \tag{A13}$$

[17] Using the WKB amplitude of a mode (see equation A3) together with the property that $l(l+1)\xi_a^h/r \sim k_r\xi_a^r \gg \xi_a^r$, it can be shown that $\gamma_a^{(\rm loc)}(\partial k_r/\partial\omega_a)$ is proportional to the integrand of equation (A5).

Downloaded from https://academic.oup.com/mnras/article/496/4/5482/5863236 by California Institute of Technology user on 22 October 2020

Plugging this into equation (A12) and contracting both sides with $\boldsymbol{\xi}_a$ then gives an alternate expression for the tidal overlap:

$$Q_a = \frac{\omega_a^2}{W_{lm} E_0} \int \left[\xi_{\rm eq}^r \xi_{\rm a}^r + l(l+1)\xi_{\rm eq}^h \xi_a^h\right] \rho r^2 {\rm d}r, \tag{A14}$$

where $\boldsymbol{\xi}_{\rm eq}$ is evaluated with $\epsilon = 1$. Also here we focus on the spatial part of $\boldsymbol{\xi}$ only (dropping the temporal phase, which is complex); for adiabatic oscillations both $\boldsymbol{\xi}_{\rm eq}(\boldsymbol{r})$ and $\boldsymbol{\xi}_a(\boldsymbol{r})$ are real.

In Fig. 3, we plot Q_a given by equation (A14). The blue dots are the exact values and the solid orange line is the asymptotic fit we use in the non-linear network calculations.

A4 Three-mode-coupling coefficient

In this section, we calculate the three-mode-coupling coefficient κ_{abc} for our WD model. For conciseness, we use $a_r(a_h)$ to represent the radial (horizontal) displacement ξ_a^r (ξ_a^h) of mode a. We further define $\Lambda_a^2 = l_a(l_a+1)$ and the angular integral,

$$T = \left[\frac{2(l_a+1)(l_b+1)(l_c+1)}{4\pi}\right]^{1/2} \times \begin{pmatrix} l_a & l_b & l_c \\ m_a & m_b & m_c \end{pmatrix} \begin{pmatrix} l_a & l_b & l_c \\ 0 & 0 & 0 \end{pmatrix}, \tag{A15}$$

where the matrices are Wigner 3-*j* symbols.

While the exact expression for the coupling coefficient is complicated (see equations A55–A62 in WAQB12), numerically we find that terms (A56) and (A58) in WAQB12 dominate (the two have about the same magnitude but opposite sign). This allows us to write

$$\begin{aligned} 2E_0 \frac{{\rm d}\kappa_{abc}}{{\rm d}r} \simeq\ & Tr\Gamma_1 P \left[\nabla\cdot\boldsymbol{b}\nabla\cdot\boldsymbol{c}\left(\Lambda_a^2 a_h - 4a_r\right)\right. \\ & \left. + \nabla\cdot\boldsymbol{c}\nabla\cdot\boldsymbol{a}\left(\Lambda_b^2 b_h - 4b_r\right) + \nabla\cdot\boldsymbol{a}\nabla\cdot\boldsymbol{b}\left(\Lambda_c^2 c_h - 4c_r\right)\right] \\ & + 4Trg\rho\left(\nabla\cdot\boldsymbol{a}b_r c_r + \nabla\cdot\boldsymbol{b}c_r a_r + \nabla\cdot\boldsymbol{c}a_r b_r\right), \end{aligned} \tag{A16}$$

where we use the fact that $4g \gg r{\rm d}g/{\rm d}r$. We further simplify this equation by substituting

$$\Gamma_1 P \nabla\cdot\boldsymbol{\xi} \simeq g\rho\xi_a^r - \omega_a^2 r\rho\xi_a^h \simeq g\rho\xi_a^r, \tag{A17}$$

where in the first equality we make the Cowling approximation and in the second we use the fact that $g \sim \omega_0^2 r \gg \omega_a^2 r$. We then have

$$\begin{aligned} 2E_0 \frac{{\rm d}\kappa_{abc}}{{\rm d}r} &\simeq Tr\frac{P}{\Gamma_1 H^2}\left(\Lambda_a^2 a_h b_r c_r + \Lambda_b^2 b_h a_r c_r + \Lambda_c^2 c_h a_r b_r\right) \\ &\simeq Tr\frac{P}{\Gamma_1 H^2}\Lambda_a^2 a_h b_r c_r, \end{aligned} \tag{A18}$$

where H is the pressure scale height. We keep only the $b_r c_r$ term for the reason given in WAQB12. Namely, for high-order modes $b_r c_r \propto \sin(\phi_b)\sin(\phi_c) = \cos(\phi_b - \phi_c)/2 \simeq 1/2$, which is roughly a constant given that $\phi_b \simeq \phi_c$. By comparison, the $b_r c_h$ term is much smaller since $b_r c_h \propto \sin(\phi_b - \phi_c)/2 \ll 1$ for $\phi_b \simeq \phi_c$. Although for the WD model we start from a different point than WAQB12 for solar-type stars (the sum of equations A56 and A58 instead of equation A56 alone), the final result we obtain reduces to equation (A63) in WAQB12.

In the top panel of Fig. A2, we show the cumulative three-mode-coupling coefficient $\int^r {\rm d}r({\rm d}\kappa_{abc}/{\rm d}r)$. The solid grey line is the result found by integrating all the terms in the exact expression for κ_{abc} given in WAQB12, and the dashed grey line is the result found by integrating the approximate expression given by equation (A18).

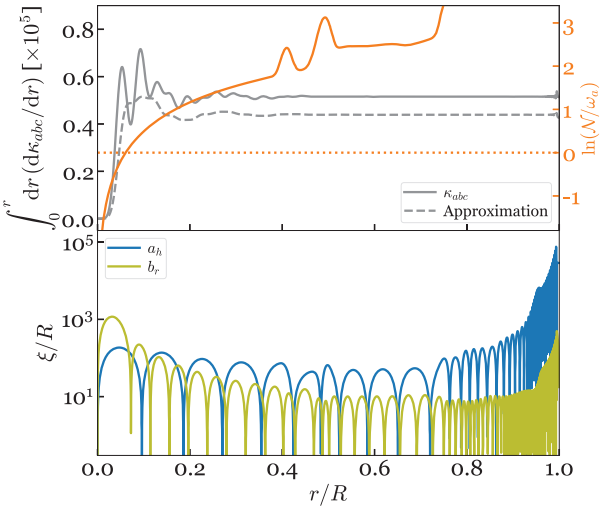

Figure A2. Top panel: cumulative three-mode coupling $\int^r {\rm d}r({\rm d}\kappa_{abc}/{\rm d}r)$ (grey traces) and $\ln(\mathcal{N}/\omega_a)$ (orange traces). Note that most of the (global) mode coupling happens in the region $r \lesssim 0.1R$ despite the fact that the local shear peaks near the surface. Bottom panel: Lagrangian displacement of the parent mode's horizontal component a_h (blue) and one of the daughter modes' radial component b_r (olive).

Here the parent mode quantum numbers are $(l_a, m_a, n_a) = (2, 2, 47)$ and the daughters are $(l_b, m_b, n_b) = (2, 0, 94)$ and $(l_c, m_c, n_c) = (2, -2, 96)$.

Note that the three-mode coupling accumulates primarily in the core region (at $r \lesssim 0.1R$), near the inner boundary of the wave's propagation where $\omega_a \simeq \mathcal{N}$ (see orange line in Fig. A2). By contrast, the shear and linear damping peak near the surface of the star where the modes are highly oscillatory (see Fig. A1).

We also show the horizontal displacement of the parent mode a_h (blue) and the radial displacement of one of the daughters b_r (olive) in the lower panel of Fig. A2. Comparing with the top panel, we see that most of the contribution to three-mode coupling happens near the parent's inner turning point. In this region the parent transitions from being oscillatory to evanescent and the coupling adds coherently over a length scale of order $\simeq 0.1R$ (although the parent is also evanescent at its outer turning point, that region contributes little to the global coupling since it is very near the surface where the density is small). As we note above, since the daughters are spatially coherent, $b_r c_r \approx$ constant, and it is the parent's spatial variations that matters most.

In Fig. 4, we show the coupling coefficient as a function of the parent mode's radial order (bottom axis) and frequency (top axis). The blue dots (κ_{abc}) are coefficients evaluated with the exact expression for daughter pairs with the smallest frequency detuning to the parent mode and satisfying $|n_b - n_c| < n_a$, and the orange dots (κ_{abb}) are evaluated for the most-resonant, self-coupled daughters (i.e. $b = c$). Here we restricted the daughters to have $l = 2$, although the coupling to daughters with different l's is similar. Indeed, as long as $|n_b - n_c| \lesssim n_a$, the coupling coefficients are approximately the same (after factoring out the angular dependence T) and can be treated as a function of the parent mode's (l_a, n_a) alone (see also Wu & Goldreich 2001; WAQB12). We also show the coupling coefficient evaluated with the approximate expression equation (A18) for self-coupled daughters (green dots). Lastly, the purple line is the asymptotic fit given by equation (24).

Downloaded from https://academic.oup.com/mnras/article/496/4/5482/5863236 by California Institute of Technology user on 22 October 2020

APPENDIX B: SPIN EVOLUTION WITH DIFFERENT NON-LINEAR DISSIPATION MODELS

In the main text we use Model 2 (M2) as our fiducial model for the tidal dissipation rate (Section 5.3.3). While M2 provides a good fit to the numerical results, near the resonance peaks Model 1 (M1; Section 5.3.2) provides a somewhat better fit (see Fig. 9), albeit at the expense of a less simple analytic form. Here we compare the two models and show that they give similar results.

In Fig. B1, we show the M1 (orange lines) and M2 (blue line) trajectories for the evolution of the WD's spin and heating rates (similar to Fig. 11). We see that they are very similar overall. There are, however, two noticeable differences. First, the critical orbital period P_c when $T_s = T_{gw}$ is first satisfied is smaller for M1 than M2. This is because the maximum torque provided by a given parent mode is smaller in M1 than in M2 (see Fig. 9). Therefore, P_c corresponds to a smaller radial order n_a of the parent mode in M1 than in M2. This also slightly reduces the temporal density and depth of the dips as both the mode density and the peak-to-trough spread of the dissipation rate (see Fig. 10) decrease with decreasing n_a. Second, whereas in M2 the dips are single narrow lines that occur each time tidal synchronization is lost and the resonance transitions to a new mode, in M1 the dips are line doublets. This is because in M1, $\dot{E}_{diss}$ has a more complicated dependence on parent detuning Δ_a; unlike M2 the peak $\dot{E}_{diss}$ is not at $\Delta_a = 0$ but instead at the shoulders with $\Delta_a \simeq \gamma_{eff}$ (see Fig. 9). The major dip is still due to the transition from one resonant mode to the other (the same as in M2). The minor dip is due to the decrease of dissipation rate at exact resonance (with $\Delta_a = 0$) compared to at the shoulder (with $\Delta_a \simeq \gamma_{eff}^{(M1)}$). The minor dips are not in the middle of two major ones because while $\dot{E}_{diss}$ is symmetric about the resonance, the GW decay rate increases monotonically as P_{orb} decreases.

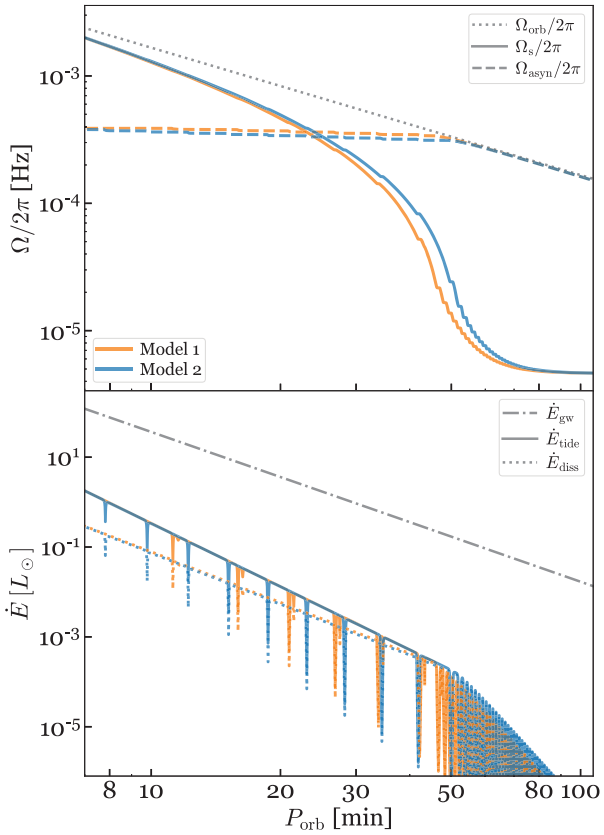

Figure B1. Similar to Fig. 11 but now also showing the results of Model 1 (orange lines) in order to compare with Model 2 (blue lines).

APPENDIX C: TRAVELING-WAVE SOLUTION

In the main text we compare the linear traveling-wave results studied previously to our weakly non-linear standing wave results. In this appendix, we describe the traveling-wave solution of the dynamical tide in more detail. Our approach closely follows that presented in FL12.

To linear order, the inhomogeneous equations describing the perturbed fluid flow are (see e.g. Lai 1994)

$$\left(r^2\xi^r\right)' = \frac{g}{c_s^2} r^2 \xi^r + \left[\frac{l(l+1)}{\omega^2} - \frac{r^2}{c_s^2}\right]\frac{\delta P}{\rho} + \frac{l(l+1)}{\omega^2} U, \tag{C1}$$

$$\left(\frac{\delta P}{\rho}\right)' = (\omega^2 - \mathcal{N}^2)\xi^r + \frac{\mathcal{N}^2}{g}\left(\frac{\delta P}{\rho}\right) - U', \tag{C2}$$

$$\xi^h(r) = \frac{1}{\omega^2 r}\left[\frac{\delta P}{\rho} + U\right], \tag{C3}$$

where primes denote partial derivatives with respect to radius, ω is the tidal forcing frequency, δP is the Eulerian pressure perturbation, and in this section $U = U(r) = -W_{lm}(GM'/D)(r/D)^l$ is the radial dependence of the tidal potential. We neglect perturbations to the gravitational potential of the primary, i.e. we make the Cowling approximation, which is reasonable given the short wavelength of the dynamical tide for the orbital periods of interest.

The displacement field can be expressed as sum of equilibrium tide and dynamical tide components, i.e. $\xi^r = \xi^r_{eq} + \xi^r_{dyn}$, and similarly for the horizontal displacement, where in the Cowling approximation,

$$\xi^r_{eq} = -\frac{U}{g}, \tag{C4}$$

$$\xi^h_{eq} = -\frac{1}{l(l+1)r}\left(\frac{r^2 U}{g}\right)'. \tag{C5}$$

In the traveling-wave limit, the shear at the outer boundary is assumed to be sufficiently large that the dynamical tide component breaks locally at the location where $k_r\xi^r$ peaks (see Fig. A1). To ensure that

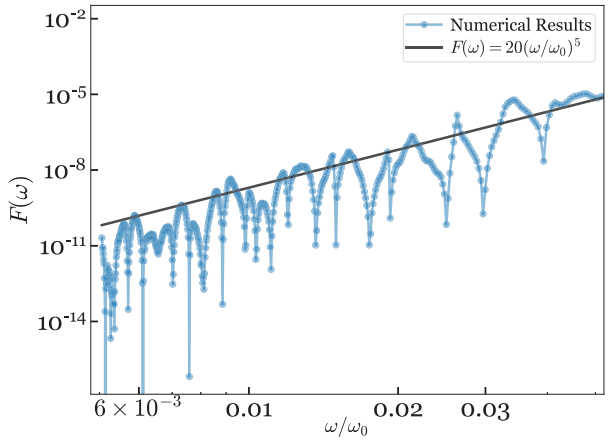

Figure C1. The traveling-wave tidal torque function $F(\omega)$ as a function of $\omega = m(\Omega_{orb} - \Omega_s)$ (blue circles; see equation C9). The black line shows the approximation $\hat{f}(\omega/\omega_0)^5$ with $\hat{f} = 20$. The result is in good agreement with the calculation in FL12 for a similar WD model.

Downloaded from https://academic.oup.com/mnras/article/496/4/5482/5863236 by California Institute of Technology user on 22 October 2020

only an outgoing wave exists, we impose a radiative outer boundary condition at the peak of $k_r\xi^r$ (corresponding to $r \simeq 0.994R$ for the $T_{\rm eff} = 9000\,{\rm K}$ WD model) given by

$$\left(\xi^h - \xi^h_{\rm eq}\right)' = \left[\frac{-(\rho r^2/k_r)'}{2(\rho r^2/k_r)} - {\rm i}k_r\right]\left(\xi^h - \xi^h_{\rm eq}\right). \tag{C6}$$

At the inner boundary we apply the regularity condition $\omega^2 r\xi^r = \delta P/\rho + U$. The set of inhomogeneous equations (C1)–(C3) can then be solved to obtain the perturbed displacement field.

The wave carries a net angular momentum flux,

$$\dot{J}_z(r) = 2m\omega^2\rho r^3 {\rm Re}\left[{\rm i}\left(\xi^r_{\rm dyn}\right)^* \xi^h_{\rm dyn}\right], \tag{C7}$$

which becomes a positive constant near the outer boundary since the wave is purely outgoing. This constant corresponds to the tidal torque exerted on the star, which can be expressed as

$$\tau_{\rm tide} = E_0\left(\frac{y}{1+y}\right)^2\left(\frac{\Omega_{\rm orb}}{\omega_0}\right)^4 F(\omega), \tag{C8}$$

where the function $F(\omega)$ can be approximated as (equation 78 in FL12)

$$F(\omega) \simeq \hat{f}\left(\frac{\omega}{\omega_0}\right)^5, \tag{C9}$$

with $\hat{f}$ a dimensionless constant that depends on the internal structure of the WD.

In Fig. C1, we show the numerical calculation of $F(\omega)$ (blue dots) and the approximation given by equation (C9) for our $T_{\rm eff} = 9000\,{\rm K}$ WD model (solid grey line). We find that $\hat{f} = 20$ provides a reasonable fit to the numerical result. This agrees well with the results of FL12 for their $0.6\,{\rm M}_\odot$ WD model with $T_{\rm eff}$=8720 K.

To understand the scaling of the traveling-wave shear shown in Fig. 6, we first note that near the surface, the horizontal and radial components of the wave satisfies (FL12)

$$\xi^h_{\rm dyn} = -{\rm i}\frac{k_r r}{l(l+1)}\xi^r_{\rm dyn} \propto \frac{\xi^r_{\rm dyn}}{\omega}. \tag{C10}$$

Combining this with equations (C7)–(C9) gives

$$\xi^r_{\rm dyn} \propto \Omega^2_{\rm orb}\omega^2 \text{ and } k_r\xi^r_{\rm dyn} \propto \Omega^2_{\rm orb}\omega. \tag{C11}$$

For a non-rotating WD, $\omega = 2\Omega_{\rm orb}$, and we obtain the $P^{-3}_{\rm orb}$ scaling shown in Fig. 6.

This paper has been typeset from a TEX/LATEX file prepared by the author.

Downloaded from https://academic.oup.com/mnras/article/496/4/5482/5863236 by California Institute of Technology user on 22 October 2020